Non-Hermitian topology and flat bands via an exact real-space decimation scheme

Ayan Banerjee,[1,*,†] Arka Bandyopadhyay,[1,*] Ronika Sarkar,[1,2,*] and Awadhesh Narayan[1,‡]
[1]*Solid State and Structural Chemistry Unit, Indian Institute of Science, Bangalore 560012, India*
[2]*Department of Physics, Indian Institute of Science, Bangalore 560012, India*

(Received 1 November 2023; revised 8 August 2024; accepted 14 August 2024; published 27 August 2024)

In recent years, non-Hermitian phases in classical and quantum systems have garnered significant attention. In particular, their intriguing band geometry offers a platform for exploring unique topological states and unconventional quantum dynamics. However, their topological characterization becomes particularly interesting and challenging in complex multiband systems. Here we propose a decimation framework, which leverages real-space renormalization group to streamline the analysis of complex multiband non-Hermitian systems. Our systematic approach allows us to probe different phases and transitions, analyze bulk-boundary correspondence, formulate generalized Brillouin zones, investigate open boundary spectra, survey non-Bloch van Hove singularities, study disorder-induced effects, and explore tunable non-Hermitian flat-band physics. Additionally, our framework allows proposing a hypothesis about quasi-one-dimensional bipartite non-Hermitian systems with flat bands, demonstrating their decoupling into Su-Schrieffer-Heeger chains and compact localized states across various models. Our paper presents a powerful and comprehensive framework for understanding the intricate properties of non-Hermitian multiband systems, offering insights into the evolving landscape of non-Hermitian topological physics.

DOI: 10.1103/PhysRevB.110.085431

I. INTRODUCTION

The exploration of non-Hermitian phases in open classical and quantum systems has gained significant traction in both theoretical and experimental realms [1–5]. Non-Hermiticity enriches and offers unique topological phases considering the interplay between ramified symmetries and topology [6,7]. The presence of exceptional degeneracies in non-Hermitian systems leads to intriguing spectral topology, facilitating non-Hermitian phase transitions and introducing the notion of "point" and "line" gap topologies in the complex plane [8,9]. The spectral topology and its extreme sensitivity to boundary conditions give rise to interesting phenomena such as the non-Hermitian skin effect (NHSE) [10,11]. This, in turn, has led to exciting applications such as enhanced lasing [12], topological funnelling of light [13], unique unidirectional transport [14,15], among several others. Non-Hermitian flat bands, characterized by their peculiar properties and correlations, offer a rich platform for exploring intriguing phenomena such as unique topological states, nonreciprocal transport, and unconventional quantum dynamics, challenging conventional band structures and expanding our understanding of correlated physics [15–17]. On the other hand, the spectral topology and concomitant topological characterization in terms of an appropriate topological invariant become more interesting as well as challenging when the system has enhanced degrees of freedom and multiple ($n \geqslant 3$) number of energy bands [18,19]. Recent progress in both theoretical and experimental activities that explore the physics of non-Hermitian multiband systems are quickly altering the research landscape [16,20–22]. Given the recent developments, there is a need for a general approach that can offer a more profound theoretical understanding of these complex multiband systems.

In this paper, we propose a complementary non-Hermitian framework based on a decimation scheme [23–25], which serves as a backbone of the scale transformation in the real-space renormalization group (RSRG) framework [26–29]. More specifically, our formalism is *exact* and utilizes the power of renormalization group theory to integrate out the chosen degrees of freedom, resulting in the downfolding of a complex Hamiltonian. In other words, our method efficiently maps the original system to a smaller, simplified yet self-contained system, which retains the information regarding the band theoretic and associated topological properties through its coarse-grained renormalized parameters.

The formalism proposed here is a powerful tool for streamlining the analysis of complex multiband non-Hermitian systems. Our systematic approach has yielded intriguing results, including: (i) Probing different phases and phase transitions of generalized non-Hermitian multiband models; (ii) analyzing the bulk-boundary correspondence (BBC) using a transfer matrix approach; (iii) formulating a generalized Brillouin zone (GBZ) for a complex multiband system; (iv) investigating open boundary spectra and skin modes; (v) surveying non-Bloch van Hove singularities; (vi) studying the effect of impurity and disorder in transport properties; and (vii) exploring tunable non-Hermitian flat-band physics using a general prescription. Additionally, our approach also sheds light on the qualitative understanding of compact

*These authors contributed equally to this work.
†Contact author: ayanbanerjee@iisc.ac.in
‡Contact author: awadhesh@iisc.ac.in

localized states (CLS) in non-Hermitian systems. In particular, we hypothesize that *any quasi-one-dimensional (Q1D) bipartite non-Hermitian system exhibiting a flat band can be decoupled into a non-Hermitian Su-Schrieffer-Heeger (SSH) chain and periodically arranged isolated sites.* The non-Hermitian SSH chain enables the band topology, while the latter manifests the nondispersive band. Our hypothesis is tested for different Q1D non-Hermitian lattice models. Furthermore, we demonstrate the versatility of the real-space decimation strategy across diverse models, including higher-order topological insulators, interfaces between Hermitian and non-Hermitian systems, and systems with long-range hopping. We show that by calculating the density of states using the Green's function formalism for large systems with long-range hopping, the decimation approach is computationally much less expensive than using the original Hamiltonian, as the renormalized Hamiltonian is significantly smaller. Similarly, for transport property calculations, such as transmittance, the decimation scheme proves to be a computationally efficient tool. Therefore, the decimation scheme is an exact transformation that is highly advantageous for exploring the underlying physics of various interesting and unique properties of non-Hermitian systems through analytical descriptions. Its field of application is broad, and for some complex, large multiband systems, the downfolding method is also found to be computationally less expensive compared to the original Hamiltonian. Overall, our formalism offers a comprehensive framework for studying and understanding the properties of complex multiband non-Hermitian systems.

II. FORMALISM

The tight-binding Hamiltonian for a noninteracting fermionic system can be expressed in the tight-binding representation as

$$\hat{H} = \sum_{n} |n\rangle \tilde{\epsilon}_n \langle n| + \sum_{n \neq m} |n\rangle \tilde{V}_{nm} \langle m|, \tag{1}$$

where the complex variables $\tilde{\epsilon}_n$ represent the on-site energies, while $\tilde{V}_{nm}$ denote the transfer (hopping) energy between the orbitals $|n\rangle$ and $|m\rangle$. Furthermore, the equation of motion for the Green's function can be derived using the tight-binding Hamiltonian provided and is expressed as $\sum_l (E\delta_{nl} - H_{nl})G_{lm}(E) = \delta_{nm}$. In the case of non-Hermitian systems, the retarded electronic Green's function G^R has the form $G^R(E) = [E + i\eta - H_0 - \Sigma(E)]^{-1}$, where H_0 and Σ represent the bare single-particle Hamiltonian and the impact of non-Hermiticity on the system, respectively [30]. Further, Σ can characterize the self-energy in a many-body scenario where the quasiparticles have a finite lifetime [30]. Additionally, it can capture the presence of gain and loss terms in an effective non-Hermitian Hamiltonian, particularly when describing an open system coupled to a bath with appropriate time dynamics [31].

For a lattice model, a preferred subset of "degrees of freedom" (or variables) can be eliminated from the original set of linear equations for the Green's function. In principle, the decimation process can be an iterative process that systematically coarse grains the parameter space; however, it yields the exact full density of states (DOS) [23]. In a similar vein,

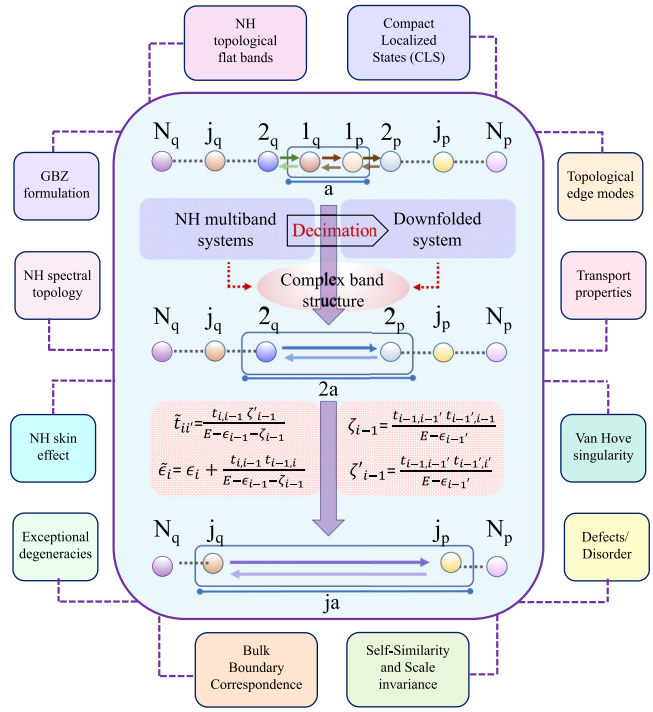

FIG. 1. Application of the decimation scheme in non-Hermitian physics. Schematic representation of the real-space decimation scheme to down-fold a non-Hermitian Hamiltonian. Initially, different blocks of lattice sites ($n_{p/q}$, where $n = 1, 2, 3, ...N$) are interconnected by nonreciprocal hopping matrices marked by solid and dashed arrows. Each block can include both gain and loss terms and nonreciprocal intrablock hopping matrices. Each decimation step invariably reduces the number of blocks but at the expense of renormalized tight-binding parameters. The modified parameters are also shown for a general ith step decimation process. The downfolded lattice precisely mimics both the real and imaginary spectra of the original non-Hermitian model. The potential application of this technique in revealing numerous properties of a non-Hermitian system are also highlighted.

here, we shall explore how the degree of complexity of any non-Hermitian multiband system can be substantially reduced by downfolding the corresponding Hamiltonian matrix. For a comprehensive understanding of the approach, let us consider a linear chain comprising a total of $N_p + N_q$ blocks, as depicted in Fig. 1, containing information about the nonreciprocal hopping and on-site gain and loss terms. These blocks can correspond to either a single site or a collection of sites for which the tight-binding analog of the Schrödinger equation can be written as

$$(E - \epsilon_i)\phi_i = \sum_j t_{ij}\phi_j, \tag{2}$$

where $E\,\mathbb{I}$, ϵ_i, ϕ_i. and t_{ij} matrices represent the eigenenergy, on-site potential and probability amplitude at the ith block, and hopping parameter between ith and jth block, respectively.

In the case of a linear tight-binding chain, as given in Fig. 1, the difference equations given in Eq. (2) can be written

as

$$\begin{aligned}(E-\varepsilon_{1p})\psi_{1p} &= t_{1p,1q}\psi_{1q}+t_{1p,2p}\psi_{2p},\\ (E-\varepsilon_{1q})\psi_{1q} &= t_{1q,1p}\psi_{1p}+t_{1q,2q}\psi_{2q},\\ (E-\varepsilon_{2p})\psi_{2p} &= t_{2p,1p}\psi_{1p}+t_{2p,3p}\psi_{3p},\\ (E-\varepsilon_{2q})\psi_{2q} &= t_{2q,1q}\psi_{1q}+t_{2q,3q}\psi_{3q}.\end{aligned} \tag{3}$$

Using the first two equations in Eq. (3), we obtain

$$\begin{aligned}(E-\varepsilon_{1p})\psi_{1p} = t_{1p,1q}\left[\frac{t_{1q,1p}}{E-\varepsilon_{1q}}\psi_{1p}+\frac{t_{1q,2q}}{E-\varepsilon_{1q}}\psi_{2q}\right]\\ +t_{1p,2p}\psi_{2,p}\end{aligned} \tag{4}$$

In other words,

$$(E-\varepsilon'_{1p})\psi_{1p} = t'_{1p,2q}\psi_{2q}+t_{1p,2p}\psi_{2p}. \tag{5}$$

Here $\varepsilon'_{1p}=\varepsilon_{1p}+\frac{t_{1p,1q}\cdot t_{1q,1p}}{E-\varepsilon_{1q}}$ and $t'_{1p,2q}=\frac{t_{1p,1q}\cdot t_{1q,2q}}{E-\varepsilon_{1q}}$.
Similarly, the difference equation for $\psi_{1,q}$ takes the form

$$(E-\varepsilon'_{1q})\psi_{1q} = t'_{1q,2p}\psi_{2p}+t_{1q,2q}\psi_{2q}, \tag{6}$$

where, $\varepsilon'_{1q}=\varepsilon_{1q}+\frac{t_{1q,1p}\cdot t_{1p,1q}}{E-\varepsilon_{1p}}$ and $t'_{1q,2p}=\frac{t_{1q,1p}\cdot t_{1p,2p}}{E-\varepsilon_{1p}}$.

Next, we substitute Eqs. (5) and (6) in the third and fourth equations of Eq. (3), obtaining

$$\begin{aligned}(E-\varepsilon'_{2p})\psi_{2p} &= t'_{2p,2q}\psi_{2q}+t_{2p,3p}\psi_{3p},\\ (E-\varepsilon'_{2q})\psi_{2q} &= t'_{2q,2p}\psi_{2p}+t_{2q,3q}\psi_{3q},\end{aligned} \tag{7}$$

where $\varepsilon'_{2p}=\varepsilon_{2p}+\frac{t_{2p,1p}\cdot t_{1p,2q}}{E-\varepsilon'_{1p}}$, $t'_{2p,2q}=\frac{t_{2p,1p}\cdot t'_{1p,2p}}{E-\varepsilon'_{1p}}$, $\varepsilon'_{2q}=\varepsilon_{2q}+\frac{t_{2q,1q}\cdot t_{1q,2p}}{E-\varepsilon'_{1q}}$, and $t'_{2q,2p}=\frac{t_{2q,1q}\cdot t'_{1q,2p}}{E-\varepsilon'_{1q}}$.

In effect, we have decimated the information of $1_{p/q}$ sites into the remaining tight-binding parameters. Furthermore, we have downfolded the system to a one-step decimated version of the extensive system with difference equations for $2_{p/q}$ in terms of renormalized coupling parameters. This scheme is an iterative process that can be performed for any number of decimation steps. The flow equation to obtain the transformed tight-binding parameters ($\tilde{\epsilon}_k$, $\tilde{t}_{kl}$) in order to derive the renormalized parameters can be written as follows:

$$\begin{aligned}\tilde{\epsilon}_i &= \epsilon_i+\frac{t_{i,(i-1)}t_{(i-1),i}}{E-\epsilon_{(i-1)}-\frac{t_{(i-1),(i-1)'}t_{(i-1)',(i-1)}}{E-\epsilon_{(i-1)'}}},\\ \tilde{t}_{i,i'} &= \frac{t_{i,(i-1)}\,t_{(i-1),(i-1)'}\,t_{(i-1)',i'}}{(E-\epsilon_{(i-1)'})\left[E-\epsilon_{(i-1)}-\frac{t_{(i-1),(i-1)'}t_{(i-1)',(i-1)}}{E-\epsilon_{(i-1)'}}\right]}.\end{aligned} \tag{8}$$

In the above Eq. (8), the p and q sites are represented by primed and unprimed parameters and should be interchanged for $p\leftrightarrow q$. This decimation scheme is an iterative process, and the non-Hermitian Green's function can readily be calculated from the renormalized Hamiltonian at each decimation step. In other words, the entire system information can be encoded into an effective two-site problem containing decimated on-site parameters of N_p and N_q and hopping parameters between the same. However, in this case, the most pertinent question remains—Can the real-space decimation scheme capture the complete complex multiband topology? Next, we present a comprehensive resolution to this question at hand.

III. NON-HERMITIAN BAND TOPOLOGY THROUGH DECIMATION

To answer the aforementioned question, we consider a non-Hermitian four-band model featuring both nonreciprocal hopping and inversion symmetric imaginary potentials, as illustrated in Fig. 2. The Hamiltonian is $H=H_{\rm hop}+H_{\rm pot}$, where the individual terms are given by [32]

$$\begin{aligned}H_{\rm hop} &= -\sum_j[t_1(c^\dagger_{j,A}c_{j,B}+\text{H.c.})+t_2(c^\dagger_{j+1,A}c_{j,B}+\text{H.c.})]\\ &\quad+\sum_j\tau(c^\dagger_{j,B}c_{j,A}-c^\dagger_{j,A}c_{j,B}),\\ H_{\rm pot} &= i\gamma\sum_j(c^\dagger_{2j-1,A}c_{2j-1,A}+c^\dagger_{2j,B}c_{2j,B}-c^\dagger_{2j,A}c_{2j,A}\\ &\quad-c^\dagger_{2j-1,B}c_{2j-1,B}),\end{aligned} \tag{9}$$

where $c^\dagger_{j,\alpha}(c_{j,\alpha})$ are the fermionic creation (annihilation) operators for the sublattice $\alpha=A,B$, and the lattice site is indexed by j [see Fig. 2(a)]. The term $H_{\rm hop}$ with nonreciprocal intra-unit-cell hopping $t_1\pm\tau$ and inter-unit-cell coupling t_2 describes the two sublattices in the non-Hermitian Su-Schrieffer-Heeger (SSH) model. Additionally, we introduce $H_{\rm pot}$, i.e., the imaginary staggered potential that respects inversion symmetry. The system Hamiltonian of the lattice in Bloch space is obtained as

$$H_k=\begin{pmatrix} i\gamma & t_1-\tau & 0 & t_2e^{-ik}\\ t_1+\tau & -i\gamma & t_2 & 0\\ 0 & t_2 & -i\gamma & t_1-\tau\\ t_2e^{ik} & 0 & t_1+\tau & i\gamma\end{pmatrix}. \tag{10}$$

The selection of the generalized non-Hermitian SSH model as our focus is particularly appropriate, considering the extensive research dedicated to both $H_{\rm hop}$ and $H_{\rm pot}$ individually. This choice allows us to leverage the substantial body of knowledge on these models [33–40] and explore its intriguing physics within the context of the RSRG decimation scheme. The system described by the Hamiltonian, $H=H_{\rm hop}+H_{\rm pot}$, has a discrete translational symmetry. Furthermore, the Bloch Hamiltonian, H_k, in the momentum space respects the ramified particle-hole symmetry (PHS†) denoted by the unitary matrix $\hat{\mathcal{S}}_-$ [6]. The PHS† operator is defined by: $\hat{\mathcal{S}}_-H^*_k\hat{\mathcal{S}}_-^{-1}=-H_{-k}$, where $\hat{\mathcal{S}}_-=\sigma_0\otimes\sigma_z$.

We move on to the real space and employ the decimation scheme to decimate the four-band model to obtain an effective two-band model with renormalized energy-dependent coupling and on-site (gain/loss) terms. We will show that this two-band model can precisely mimic the original system, capturing all its essential physics, and also decipher the known phase diagram for $\tau=0$ as a special case (see Appendix A for details). Next, we present a systematic study of the decimated model and the underlying non-Hermitian phase transitions as a function of nonreciprocity, τ, and gain-and-loss coefficient, γ.

We have judiciously integrated out the middle two (green) sites from the original lattice [see Fig. 2(a)]. In particular, we have obtained the following coupled equations, $[E-\epsilon'']\phi_a=\Theta\phi_d+t_2\phi'_d$ and $[E-\epsilon'']\phi_d=\Theta'\phi_a+t_2\phi'_a$. This yields an effective two-band model with energy-dependent renormalized

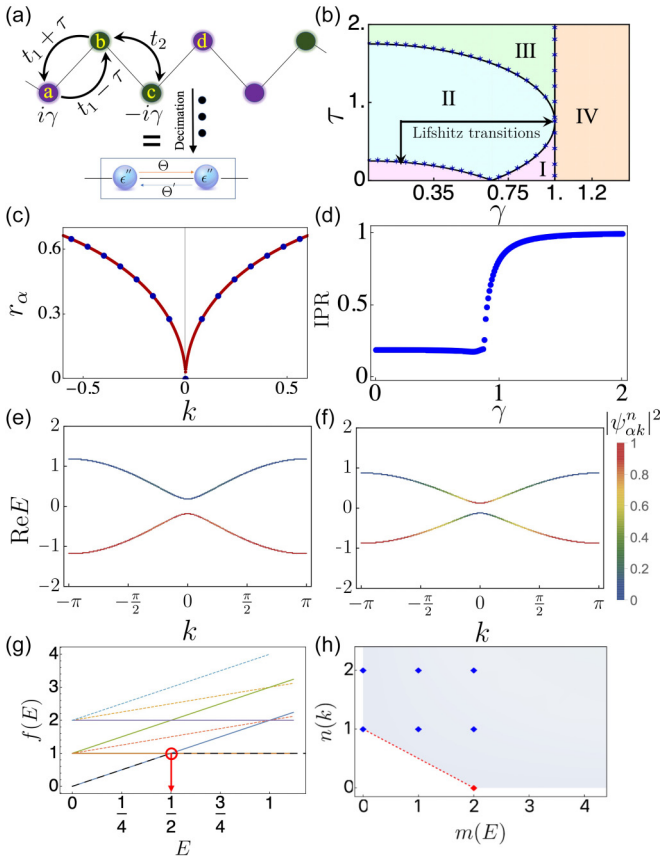

FIG. 2. Analysis of NH spectral topology in a generalized SSH chain through decimation scheme. (a) Illustration of the decimation scheme for the generalized SSH chain [see Eq. (9)] to obtain a downfolded two-site model, which encodes the essential topological information of the NH spectral topology of the original model. (b) Phase diagram of the model illustrating four phases undergoing Lifshitz transition with distinct point and line gap topology. (c) The phase boundaries are the locus of the exceptional points characterized by phase rigidity. The comparison of phase rigidity (based on eigenvector scaling) obtained from the decimated model (blue dots) and the parent model (solid-red line) is also shown, which reveals a striking resemblance. (d) At the $\tau = 0$ limit, the system encounters an SSH-like (Hermitian) topological phase transition governed by real-energy gap closing. The topological real-energy zero modes under the low energy approximation can be traced out by IPR from the decimated model. For instance, we plot the IPR corresponding to real-energy zero mode, and the finite jump in the IPR around γ_c indicates trivial to topological phase transitions giving rise to localized zero-energy modes under open boundary conditions. Furthermore, the orbital character evaluated from the decimated model demarcates the trivial (e) and nontrivial phases (f) of the system with a characteristic twist around $k = 0$, which further reveals the SSH-like phase transitions with the gap closing at γ_c. We characterize the second-order exceptional points along the phase transition lines using (g) tropical geometric framework and (h) Newton polygon formalism discussed in Appendix D. In the tropical geometric framework, the bend locus of tropicalization indicates the square root dispersion, whereas the Newton polygon formalism illustrates the same through its negative slope shown in the red-dotted line. We set $t_1 = 1.0$ and $t_2 = 0.75$.

couplings and gain and loss terms.

$$H_d = \begin{pmatrix} \epsilon'' & \Theta + t_2 e^{-ika} \\ \Theta' + t_2 e^{ika} & \epsilon'' \end{pmatrix}, \tag{11}$$

where $\epsilon'' = i\gamma + (t_1 - \tau)(t_1 + \tau)/(E - \epsilon')$, $\epsilon' = -i\gamma + t_2^2/(E + i\gamma)$, $\Theta = (t_1 - \tau)^2 t_2/[(E + i\gamma)(E - \epsilon')]$, and $\Theta' = (t_1 + \tau)^2 t_2/[(E + i\gamma)(E - \epsilon')]$.

Here, we note that the renormalized parameters given above for the four-band system, depicted in Fig. 2(a), can also be achieved using the general transformation relation given in Eq. (8). We consider a system, which comprises of a unit cell consisting of four sites, where the site indices can be represented by $a = 2q$, $b = 1q$, $c = 1p$, and $d = 2p$. We decimate the information of site b and d in terms of the renormalized parameters. For instance, by considering $i = 2$, it is straightforward from Eq. (8) to obtain

$$\tilde{\epsilon}_2 = \epsilon_2 + \frac{t_{2,1} t_{1,2}}{E - \epsilon_1 - \frac{t_{1,1'} t_{1',1}}{E - \epsilon_{1'}}},$$
$$\tilde{t}_{2,2'} = \frac{t_{2,1}\, t_{1,1'}\, t_{1',2'}}{(E - \epsilon_{1'})\left[E - \epsilon_1 - \frac{t_{1,1'} t_{1',1}}{E - \epsilon_{1'}}\right]}. \tag{12}$$

We choose $\epsilon_{1,2} = \pm i\gamma$, $t_{2,1} = (t_1 - \tau)$, $t_{1,2} = (t_1 + \tau)$, and $t_{1,1'} = t_{1',1} = t_2$ to map the system parameters as obtained in above discussion. For instance, $\tilde{\epsilon}_2$ becomes $\epsilon'' = i\gamma + (t_1 - \tau)(t_1 + \tau)/(E - \epsilon')$, where $\epsilon' = -i\gamma + t_2^2/(E + i\gamma)$, and $\tilde{t}_{2,2'}$ and $\tilde{t}_{2',2}$ take the form, $\tilde{t}_{2,2'} = \Theta = (t_1 - \tau)^2 t_2/[(E + i\gamma)(E - \epsilon')]$ also $\tilde{t}_{2',2} = \Theta' = (t_1 + \tau)^2 t_2/[(E + i\gamma)(E - \epsilon')]$. We note that the choice of degrees of freedom to decimate is inherently flexible. For instance, since no spectral information from the original Hamiltonian is lost in this transformation, one option among several is to decimate the b and c sites to achieve a reduced renormalized lattice. We present a discussion illustrating a comparison between different decimation schemes in Appendix E.

The phase diagram as a function of τ and γ for this effective two-band model is shown in Fig. 2(b) (see also Appendices B and C for the band dispersion). The dispersion exactly matches the original four-band model. This alignment persists across the entire parameter range, showcasing notable phenomena such as the presence of exceptional points and topological phase transitions, which we discuss next.

The single-particle spectrum shows gap closings for absolute values of energies for lines $\pm t_2 \pm \sqrt{t_1^2 - \gamma^2}$ as well as for real energies $t_1 = \gamma$ dividing the phase diagram into four regions [see Fig. 2(b)]. We discuss various phases and their transitions as well as characterize the spectral topology using the non-Hermitian winding number in corroboration with the nondecaying chiral modes (for details, see Appendix C).

The exceptional physics occurring around the phase transition lines can be effectively characterized through a tropical geometric structure [41] and Newton polygons [42], despite the presence of energy-dependent tight-binding parameters [see Figs. 2(g) and 2(h) for the illustration and for more details see Appendix D]. To fully characterize the eigenfunctions using the decimated model, it is essential to solve

the following eigenvalue equation, $H_d(t_1, t_2, \gamma, \tau, E)\psi_d = E_d(t_1, t_2, \gamma, \tau, E)\psi_d$. We solve for the eigenvalues and eigenstates numerically. This process entails assuming different trial values of complex energy and subsequently checking which of these satisfies the characteristic equation. By systematically iterating through these trials, we are able to identify the complex energy values that correspond to the eigenvalues of interest. Thereby, we also obtain the eigenfunctions for our decimated system. In Fig. 2(c), we show the scaling of the phase rigidity, $r_d = \frac{\langle\psi_d^L|\psi_d^R\rangle}{\langle\psi_d^R|\psi_d^R\rangle}$ [43], near a phase transition line. The phase rigidity, which is solely a function of the eigenvectors, correctly reproduces the behavior of our original model [see Fig. 2(c) for a comparison with the parent model]. This further confirms the existence of an exceptional locus featuring the coalescence of eigenvectors.

At this point, it is interesting to note that in the limit $\tau \to 0$, the model corresponds to the BDI† class of the 38-fold topological classification of non-Hermitian systems, which in turn suggests that the topological phase transition of the system is governed by the closure of the real part of the energy band gaps [6,34]. To corroborate this, we analyze the low-energy limit of the decimated model and demonstrate the orbital character associated with it. The absence (presence) of characteristic twists around $k = 0$ confirms the distinction of the trivial (nontrivial) phase, as well as the existence of a critical point (γ_c) where the real energy gap closes. The closing of energy at this critical point signifies a topological phase transition [see Figs. 2(e) and 2(f); for more details, see Appendix A]. The inverse participation ratio, IPR$= \sum_\alpha |\psi_\alpha(x)|^4/(\sum_\alpha |\psi_\alpha(x)|^2)^2$, based on eigenfunction characteristics, which quantitatively measures state localization under open boundary conditions, allows us to identify and analyze the presence of localized edge modes within the system, as shown in Fig. 2(d). Even when the system is subjected to open boundary conditions, our approach begins with a simplified two-band model that incorporates energy-dependent renormalized coupling parameters. Through iterative solutions, we obtain both the eigenvalues and eigenvector structures in real space. Analyzing these eigenvectors allows us to interpret the open boundary spectra and unveil the underlying spectral topology. For example, by plotting the IPR corresponding to the zero-energy mode, we observe a distinct jump in the IPR around the critical value of $\gamma_c = \sqrt{t_1^2 - t_2^2}$. This abrupt change signifies a transition from a trivial to a topological phase, leading to the emergence of localized zero-energy modes under open boundary conditions. Non-Hermitian systems exhibit remarkable sensitivity to boundary conditions, resulting in a significant disparity between spectra under periodic (PBC) and open (OBC) boundary conditions. This broken BBC challenges conventional understanding within the Hermitian paradigm [44–46].

To investigate the effect of boundary conditions on the BBC, we consider the one-dimensional real-space tight-binding chain corresponding to the momentum-space Hamiltonian in Eq. (11). Next, we invoke OBC and evaluate the transfer matrix ($\mathcal{T}$) through the singular value decomposition of the hopping matrix [47], and in terms of the on-site Green's function (see Appendix F for details). The transfer matrix approach smoothly connects the OBC and PBC regime and characterizes the BBC through the unimodularity condition, $\det\mathcal{T} = 1$. The corresponding analysis of our decimated model gives rise to $\det\mathcal{T} = \frac{(t_1+\tau)^2}{(t_1-\tau)^2}$ (see Appendix F for the details of the calculation), which immediately suggests that in the reciprocal hopping limit ($\tau \to 0$), the BBC is restored, with identical OBC and PBC spectra. In contrast, the nonreciprocal hopping limit leads to a non-unimodular condition, indicating a disparity between OBC and PBC spectra, thus invalidating the BBC. These results align with the generalized transfer matrix approach introduced by Kunst *et al.* [47] and correspond to a special case of their method. At the vanishing determinant condition, $\det\mathcal{T} = 0$, the real-space spectrum gives rise to higher-order exceptional points with an algebraic multiplicity commensurate with the system size, whereas the geometric multiplicity remains one indicating the presence of NHSE.

To delve deeper into the physics of the skin effect in the decimated system, we adopt the non-Bloch theory with the GBZ scheme [10,48]. Here, the conventional Bloch phase factor e^{ik} is replaced by $\beta = |\beta|e^{ik}$ in the Hamiltonian, enabling a direct mapping between non-Bloch topology and open boundary spectra. This framework based on the decimated model also captures the NHSE [48,49]. The real-space eigenequation corresponding to Eq. (11) leads to the conditions, $\Theta'\psi_{a,n} + t_2\psi_{a,n+1} + \epsilon''\psi_{b,n} = E\psi_{b,n}$ and $\Theta\psi_{b,n} + t_2\psi_{b,n-1} + \epsilon''\psi_{a,n} = E\psi_{a,n}$. Analogous to Ref. [48], we consider the ansatz governed by the spatial periodicity of the system $(\psi_{a,n}, \psi_{b,n}) = \beta^n(\psi_a, \psi_b)$ and we obtain the coupled equations $\Theta'\psi_a + t_2\beta\psi_a + (\epsilon'' - E)\psi_b = 0$ and $\Theta\psi_b + t_2\beta^{-1}\psi_b + (\epsilon'' - E)\psi_a = 0$. This leads to the condition

$$g(E, \beta) = \beta^2 t_2\Theta + \beta\left\{\Theta'\Theta + t_2^2 - (\epsilon'' - E)^2\right\} + t_2\Theta' = 0, \tag{13}$$

from which β can be estimated with two solutions, β_1 and β_2, which satisfy $\beta_1\beta_2 = \Theta'/\Theta$. It can be shown that the bulk states of a long chain demand the condition, $|\beta_1| = |\beta_2|$, which eventually leads to the solution $|\beta| = |\beta_1| = |\beta_2| = \sqrt{|\Theta'/\Theta|} = \sqrt{|(t_1 + \tau)^2/(t_1 - \tau)^2|}$. Furthermore, $|\beta| < 1 (|\beta| > 1)$ corresponds to states localized at the left (right) end of the chain. We refer to Figs. 3(a) and 3(b) for an illustration of both conditions with parameter dependence $\tau < 0$ ($\tau > 0$) exhibiting the left (right) localized bulk modes. Interestingly, the occurrence of the skin effect in the different phases is evinced by the finite-spectral area (closed curves) in the complex energy plane of the decimated model under PBC (see also Appendix C) [9]. We want to point out a complementary framework that outlines general conditions for the NHSE within a non-Hermitian multiband unit cell [50]. This approach focuses on the nature of overall localization of eigenmodes, determined by the by the geometric mean of the cumulative contributions of all coupling segments. Moreover, it does not require estimating the non-Bloch band factor β, offering a straightforward approach to studying NHSE.

Next, we discuss zero-mode solutions in the low-energy approximation ($E = \epsilon''$), when Eq. (13) leads to the solutions $\beta_{1,2} = -\Theta'/t_2, -t_2/\Theta'$. The zero-energy solutions, where the bulk bands touch the zero energy, can be obtained by equating $|\beta| = |\beta_{1,2}|$, leading to the condition $t_2^2 = t_1^2 - \tau^2$. We can thereby determine the GBZ, which gives rise to continuum

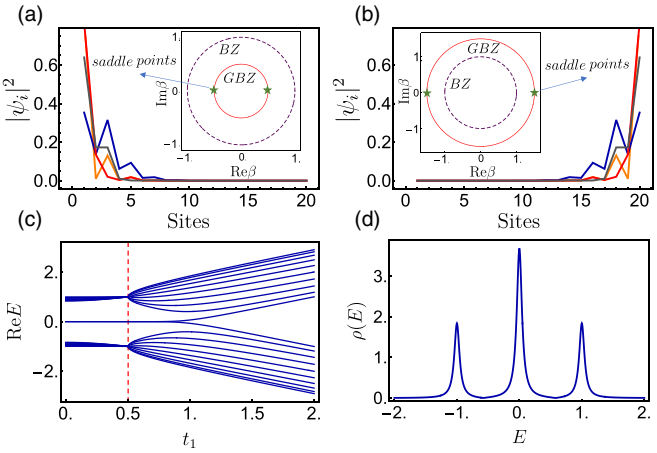

FIG. 3. Demonstration of chiral skin effect, BBC, and van Hove singularity through GBZ formulation within decimation scheme. Localization of bulk wavefunctions at (a) left ($\tau < 0$) and (b) right ($\tau > 0$) edge illustrating the NHSE. The insets show GBZ (red) and BZ (dotted black), depicting a non-unit and unit circle, respectively, in the complex plane. The radius of the GBZ greater (lesser) than unity indicates the right (left) localized states and skin effect. The GBZ becomes a unit circle with $\tau = 0$, the system restores conventional BBC. (c) $t_1 = \tau$ is the locus of the PT-symmetry breaking point with a higher order exceptional point. At this critical parameter value, the two saddle points (indicated by blue arrows) in the GBZ coalesce. Consequently, a van Hove singularity is observed in the DOS as a function of real energy.

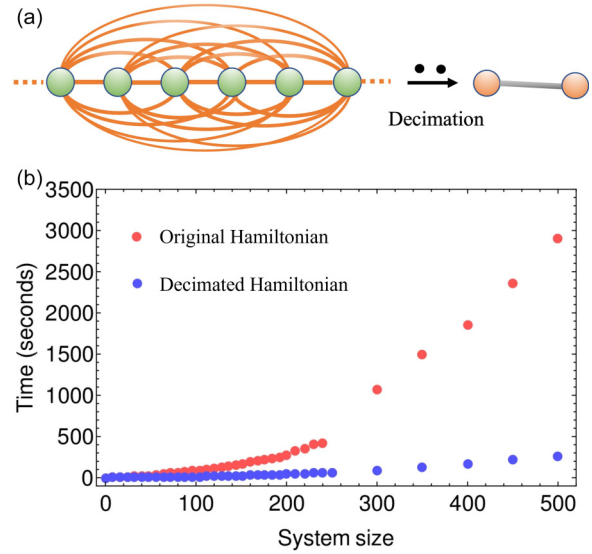

FIG. 4. Analysis of long-range power-law hopping model through decimation scheme. (a) Schematic showing a long-range model with power-law $1/l^{\alpha}$ couplings. We employ our decimation scheme to reduce the system to a two-level system with renormalized parameters and estimate the DOS using the Green's function formalism for decimated and original systems. (b) The computational time required as a function of system size. The plot reveals that the decimation scheme does not only provide conceptual simplifications but also offers computational advantages. Calculations are performed in serial mode (single processor) using 11th Gen Intel(R) Core(TM) i7-11700 @ 2.50 GHz system.

bands under the condition $|\beta_1| = |\beta_2|$ with open boundaries. Considering Eq. (13) as the kernel of non-Bloch band theory, the continuum bands can be given by solution to $g(E, \beta)$ with $z_{\mathrm{GBZ}} = \beta = |\beta|e^{ik/2}$ and $k \in [0, 2\pi)$ (see Appendices G and H). The GBZ in the complex plane describes the OBC spectrum in non-Hermitian systems with complex deformation of the momentum $k \to k + i\kappa$. Further, $\kappa = \ln|\beta|$ indicates the inverse localization length of skin modes. We next calculate the saddle points and their energies, which satisfy the condition $g(E, \beta) = 0$ and $\partial_\beta g(E, \beta) = 0$ simultaneously (see Appendix H). The saddle points $[\beta_{s(1,2)} = \pm(t_1 + \tau)/(t_1 - \tau)]$, and their coalescence leads to $t_1 = |\tau|$ and $\det\mathcal{T} = 0$, which in turn, gives rise to interesting consequences [51], which we explore in terms of the decimated model. We present a discussion of GBZ formulation in the presence of generalized next-nearest-neighbor hopping in Appendix I. The study includes cases where the GBZ deviates from the simple circular shape seen in Fig. 3, highlighting the utility of our approach in these scenarios.

In the present scenario, $\det\mathcal{T} = 0$ indicates a higher-order exceptional point encountering a PT (parity-time) symmetry transition point where the purely real energy spectra bifurcate in the complex plane [3,52]. Interestingly, the merging of saddle points corroborated by the PT transition is stipulated by a singularity in the DOS along the real axis. To substantiate this, as a byproduct of our formalism, we calculate the DOS in terms of Green's function at $t_1 = \tau$, which is the PT breaking point [see Fig. 3(c)]. The saddle point coalescence on the GBZ manifests a divergence in the DOS [see Fig. 3(d)], leading to a non-Bloch van Hove singularity [51].

Furthermore, we delve into a more intricate scenario involving generalized long-range power-law coupling to test our scheme [see Fig. 4(a) see below]. We start by considering a tight-binding model with long-range couplings under OBC. The Hamiltonian reads

$$H = \sum_{j=1}^{L-1}\sum_{l=2}^{L-j}\left(\frac{t}{l^{\alpha}}c_j^{\dagger}c_{j+l} + \mathrm{H.c.}\right). \tag{14}$$

Here $c_j^{\dagger}(c_j)$ represents the fermionic creation (annihilation) operator, L is the number of sites and the power-law decaying exponent α signifies the strength of nonlocality. We have chosen $\alpha = 2$. In order words, each site of our system is connected to all the other sites. However, the strength of coupling between two sites decay fast with the distance between them. We employ our decimation scheme to reduce this to a two-level system with renormalized parameters and estimate the DOS using the Green's function formalism for both decimated and original systems. We have encoded the information from the central $L - 2$ sites of a long-range chain with L into the remaining two terminal atomic sites. Consequently, the on-site energies and the renormalized coupling between the terminal atomic sites become energy dependent. The renormalized hopping parameter is added to the original long-range hopping between the first and Lth sites. The decimation method introduced here can also be applied to long-range systems without power-law hopping strengths. We note that the DOS of the original and the decimated systems exactly matches. Furthermore, to explore the advantages of the decimation

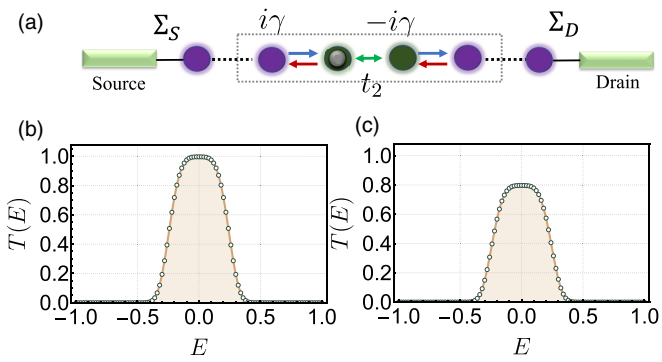

FIG. 5. Transmission probability for original and decimated systems in presence of a defect. (a) Schematic of the model for calculating the transmission probability of the non-Hermitian four-site chain. The blue (red) arrow indicates the nonreciprocal hopping $t_1 \pm \gamma$ along the right (left) direction. Ideal lossless metallic leads are used as electrodes, with source and drain with self-energy matrices Σ_S and Σ_D, respectively. The orange-solid circle represents the defect in the system. The transmission probability of the system (b) without and (c) with defect, when the system is tuned near the exceptional points. The presence of the defect invariably suppresses the transmission probability. The probability obtained from the decimated scheme (shown with blue dots) exactly matches the original model (red-solid line). Here we set $t_1 = 0.5$, $t_2 = 1.0$, $\gamma = 0.5$, $\tau = -1.0$, and $\delta_d = 1$.

scheme, the computational time required as a function of system size is shown in Fig. 4(b) below. The plot reveals that the decimation scheme does not only provide conceptual simplifications but also offers computational advantages. This analysis underscores the efficacy of our decimation strategy, providing both conceptual clarity and practical computational advantages.

Furthermore, we have investigated the transmission probability $T(E)$ through the non-Hermitian system placed between two ideal metallic electrodes, i.e., source and drain. The transmission probability can be evaluated as $T(E) = \mathrm{Tr}[\Gamma_S G(E) \Gamma_D G(E)^\dagger]$ within the Landauer-Buttiker formalism [53,54]. In the above equation, Γ_S and Γ_D can be estimated from the self-energy matrices $\Gamma_{S(D)} = i[\Sigma_{S(D)} - \Sigma^\dagger_{S(D)}]$ and therefore depend on the coupling between the electrodes and the system. In particular, we have considered the above-mentioned non-Hermitian chain having a total of $2n + 1$ unit cells (here, $n = 50$) and the parameters are so chosen that we reside near an exceptional point, i.e., $\tau = -t_2 \pm \sqrt{t_1^2 - \gamma^2}$, as schematically represented in Fig. 5(a). It is fascinating to note that the transmission probability of the original system is precisely in line with that of the decimated system [Fig. 5(b)]. The nature of the transmission probability near the exceptional point agrees well with the previous reports [55,56].

Needless to mention, the downfolding of the Hamiltonian is indeed an iterative process, and the transmission probability will be exactly the same for any decimated system size, even in the presence of any defect. To establish this, we have incorporated a defect with on-site energy δ_d, which could be present at any random lattice site. Let us consider the defect site is in the $(n+1)$th unit cell of the system with $2n + 1$ lattice sites. As we expect, the transmission probability reduces with the strength of the defect potential, which is entirely captured by both the full and decimated Hamiltonians as shown in Fig. 5(c). In the present case, the lattice sites of the remaining $2n$ unit cells have been decimated to half; however, the same methodology can be applied iteratively to reduce the lattice sites further, similar to the above case. We discussed the central features of non-Hermitian topological systems in light of the decimation scheme, and the crux of the analysis is that the complete non-Hermitian spectral topology can be encapsulated in the downfolded version of an extensive system.

IV. NON-HERMITIAN FLAT BAND THROUGH DECIMATION

Now, we discuss how the real-space decimation technique can describe the fascinating flat-band physics and emergence of compact localized states (CLSs) in non-Hermitian lattice models. As a test bed, we consider a Q1D Lieb lattice with five sites per unit cell and incorporate non-Hermiticity through on-site gain and loss [57–59]. We note that the downfolding approach presented here can be efficiently extended to any other lattice type with a flat band, where the non-Hermiticity can be of any kind, including nonreciprocal hopping. One of the realistic pathways to achieve such a non-Hermitian Lieb (nH-Lieb) lattice is to construct a photonic crystal by employing periodically arranged evanescently coupled waveguides [60]. The Hamiltonian for this five-site nH-Lieb lattice model can be written as follows:

$$\mathcal{H} = \sum_{\nu=\{a,b,c,d,e\}} \varepsilon_\nu \nu_n^\dagger \nu_n + \sum_n [a_n^\dagger(\tilde{t_1} b_n + \tilde{t_2} b_{n-1} + t c_n) + e_n^\dagger(\tilde{t_2} d_n + \tilde{t_1} d_{n-1} + t c_n) + \mathrm{H.c.}], \quad (15)$$

where $a_n^\dagger(a_n)$, $b_n^\dagger(b_n)$, $c_n^\dagger(c_n)$, $d_n^\dagger(d_n)$, and $e_n^\dagger(e_n)$ are the fermionic creation (annihilation) operator at nth unit cell for five distinct sublattices A, B, C, D and E [see Fig. 6(a)]. The parameters t, t_1, and t_2 are the coupling coefficients between different neighboring sites. Note that the lattice sites A and E are triply coordinated while the rest (B, C, and D) have coordination number two. Similar to the previous discussion, here, we aim to reduce the degree of complexity by decimating the five-site lattice to an equivalent two-level problem. For this purpose, we have first eliminated the triply coordinated sites A and E by substituting the corresponding eigenvectors ϕ_a and ϕ_e using

$$(E - \varepsilon_{a/e})\phi_{a/e} = t_1 \phi_{b/dr} + t_2 \phi_{br/d} + t\phi_c, \quad (16)$$

into the following expressions

$$(E - \varepsilon_c)\phi_c = t\phi_a + t\phi_e,$$
$$(E - \varepsilon_{b/b/d/d})\phi_{b/br/d/dr} = t_1 \phi_{a/ar/el/e} + t_2 \phi_{al/a/e/er}. \quad (17)$$

The subscripts l and r signify the sites of the nearest left and right unit cell, respectively. Figure 6(a) illustrates that this decimation process leads to an effective three-level lattice comprising of B, C, and D sites with renormalized hopping parameters given as $\lambda_{a_1} = tt_1/(E - \varepsilon_a)$, $\lambda_{a_2} = tt_2/(E - \varepsilon_a)$, $\lambda_{e_1} = tt_1/(E - \varepsilon_e)$, $\lambda_{e_2} = tt_2/(E - \varepsilon_e)$, $\lambda_{a_{12}} = t_1 t_2/(E - \varepsilon_a)$,

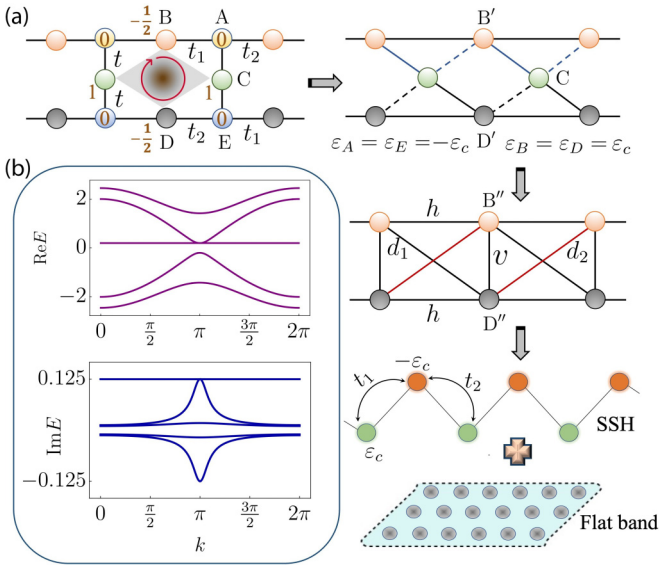

FIG. 6. Non-Hermitian flat bands through decimation. (a) Q1D Lieb lattice model with two triply coordinated (A and E) and three doubly coordinated (B, C, and D) sites. The same sites of the nearest unit cells are denoted by subscripts l and r for the left and right directions, respectively. Non-Hermiticity in the model has been incorporated through on-site gain and loss following the conditions $\varepsilon_A = -\varepsilon_B = -\varepsilon_c = -\varepsilon_D = \varepsilon_E$. The real-space decimation process reduces the lattice to an equivalent two-level non-Hermitian ladder system in two steps. First, the triply coordinated sites A and E are decimated, followed by the elimination of the C site. Finally, the ladder network is decoupled into a massive non-Hermitian SSH chain that carries the information about the topological band inversion and an array of isolated lattice sites with localized orbitals that constitute a flat band at $E = \varepsilon_c$. (b) The emergence of a flat band at a complex energy value $(0.2 + 0.125i)$ along with the massive non-Hermitian SSH-like dispersive band structure. The corresponding CLS are indicated by the gray regions in the original lattice. Note that the localization of electronic states is caused by the zero-probability amplitude of the atomic sites A and E. The parameters used here are $\varepsilon_c = 0.2 + 0.125i$ and $t_1 = t_2 = t = 1.0$.

and $\lambda_{e_{12}} = t_1 t_2/(E - \varepsilon_e)$. In addition, we also need to consider the renormalized values for the on-site energies of C, B, and D, which are $\varepsilon_c' = \varepsilon_c + t^2/(E - \varepsilon_a) + t^2/(E - \varepsilon_e)$, $\varepsilon_b' = \varepsilon_b + (t_1^2 + t_2^2)/(E - \varepsilon_a)$, and $\varepsilon_d' = \varepsilon_d + (t_1^2 + t_2^2)/(E - \varepsilon_e)$. It is evident that, as per our expectation, the new set of renormalized hopping integrals and on-site potentials depend on the decimated parameters of the original lattice. Additionally, the energy dependency of the tight-binding parameters protects the order of the characteristic equation. Now, one can execute another decimation step for further renormalizing the three-site lattice with energy-dependent parameters to an equivalent two-level system. The convenient approach, in this regard, is to choose a scheme that dissolves the information carried by the wavefunction ϕ_c into the ladder like network made up of B and D sites [Fig. 6(a)]. The final renormalized lattice contains only two types of on-site energy terms and five distinct hopping parameters given by

$$\varepsilon_b'' = \varepsilon_b' + \left(\lambda_{a_1}^2 + \lambda_{a_2}^2\right)/(E - \varepsilon_c'),$$
$$\varepsilon_d'' = \varepsilon_d' + \left(\lambda_{e_1}^2 + \lambda_{e_2}^2\right)/(E - \varepsilon_c'),$$
$$h_1 = \lambda_{a_{12}} + \left(\lambda_{a_1}\lambda_{a_2}\right)/(E - \varepsilon_c'),$$
$$h_2 = \lambda_{e_{12}} + \left(\lambda_{e_1}\lambda_{e_2}\right)/(E - \varepsilon_c'),$$
$$d_1 = \lambda_{a_1}\lambda_{e_1}/(E - \varepsilon_c'),$$
$$d_2 = \lambda_{a_2}\lambda_{e_2}/(E - \varepsilon_c'),$$
$$v = \left(\lambda_{a_1}\lambda_{e_2} + \lambda_{a_2}\lambda_{e_1}\right)/(E - \varepsilon_c'). \tag{18}$$

Therefore, the decimation process downfolds the tight-binding Hamiltonian to a 2×2 matrix at the expense of allowing new types of energy-dependent hoppings terms and on-site potentials.

In order to facilitate the understanding of the flat-band physics in this nH-Lieb lattice, let us focus on the following case, $\varepsilon_b = \varepsilon_d = \tilde{\varepsilon}$ and $\varepsilon_a = \varepsilon_e = -\tilde{\varepsilon}$ that further leads to the relations $\varepsilon_b'' = \varepsilon_d'' = \Delta$ (say), $h_1 = h_2 = h$, and $v^2 = 4d_1 d_2$. The above relations simplify the eigenvalues of the final Hamiltonian in the following form:

$$E_\pm = [\Delta + 2h\cos(k)] \pm [d_1 + d_2 + v\cos(k)]. \tag{19}$$

The above Eq. (19) apparently indicates that the coefficient $(v + 2h)$ causes the solution E_+ to be dispersive. However, by substituting all the energy-dependent parameters in the above expression and simplifying, we can show that the effective value of $(v + 2h)$ is zero. Therefore, the solution is essentially nondispersive, and the position of the flat band lies at an energy value $E = \Delta + d_1 + d_2$. In other words, the particular choice of on-site potentials $\varepsilon_a = -\varepsilon_b = -\varepsilon_d = \varepsilon_e = -\varepsilon_c$ always provides a flat band at the complex energy value $E = \varepsilon_c$, as depicted in Fig. 6(b). This eigenenergy solution is equivalent to that of periodically arranged isolated sites with energy ε_c where there is no orbital overlap between neighboring sites. The corresponding single-particle real-space eigenfunctions constitute the CLS, which can be analytically obtained using our method. In particular, solving the difference equations for a particular eigenvalue that offers a flat band will manifest the probability distribution for the CLS. In the present case of nH-Lieb lattice, probability amplitudes of different sites that manifest the CLSs are evaluated as $\phi_a = \phi_e = 0$, $\phi_b = \phi_d = -1/(t_1 + t_2)\,\phi_c$, when $E = \varepsilon_c$ and $t = 1$ as illustrated in Fig. 6(a). The missing amplitudes at sites A and E are caused by a destructive interference that yields trapping of the particles by strictly restricting the wavefunction to a particular region.

Our analytical approach reveals a fascinating consequence—the appearance of a zero-energy flat band when $\varepsilon_c = 0$. This can be further understood using the rank-nullity theorem in linear algebra [61], which states that, if $T : V \to W$ is a linear map between two finite-dimensional vector spaces, then $\dim(\mathrm{im}(T)) + \dim(\ker(T)) = \dim(V)$, where "im" and "ker" denote the image and the kernel, respectively. In other words, any matrix M of order $m \times n$ invariably satisfies the relation $\mathrm{rank}(M) + \mathrm{nullity}(M) = n$. Now, the system Hamiltonian $\mathcal{H}$ with two distinct sublattices α and β can be expressed as

$$\mathcal{H} = \begin{pmatrix} 0_{N_\alpha \times N_\alpha} & \mathcal{M}^\dagger_{N_\alpha \times N_\beta} \\ \mathcal{M}_{N_\beta \times N_\alpha} & 0_{N_\beta \times N_\beta} \end{pmatrix}. \tag{20}$$

Here, N_α and N_β denote the number of α-type and β-type sites in each unit cell, respectively. The five-site lattice [given

in Eq. (15)] consists of two triply coordinated sites (A and E) and three doubly coordinated sites (B, C, and D). Hence, in our case, $N_\alpha = 2$ and $N_\beta = 3$. Based on the above discussion, we can immediately write down the following set of equations relating rank R, and nullity Φ, [62]

$$\begin{aligned} R(\mathcal{M}) + \Phi(\mathcal{M}) &= N_\alpha = 2, \\ R(\mathcal{H}) + \Phi(\mathcal{H}) &= N_\alpha + N_\beta = 5, \\ R(\mathcal{H}) &= R(\mathcal{M}) + R(\mathcal{M}^\dagger). \end{aligned} \tag{21}$$

Using Eq. (21) and the relation $R(\mathcal{M}) = R(\mathcal{M}^\dagger)$, it is straightforward to obtain $\Phi(\mathcal{H}) = 2\,\Phi(\mathcal{M}) + 1$. Additionally, the nullity of the nonsingular matrix $\mathcal{M}$ is zero [i.e., $\Phi(\mathcal{M}) = 0$], which leads to $\Phi(\mathcal{H}) = 1$. This shows the emergence of a single zero-energy flat band, which remains pinned to sublattice β. In the present case, the above discussion leads to the amplitude distribution of the CLS, and the nonzero values are obtained only on sublattices (B, C, and D) [Fig. 6(a)].

In contrast, the other solution E_- given in Eq. (19) offers a quadratic dispersion relation from which two low-energy bands can be obtained using the relation $|E^2 - \varepsilon_c^2|/t^2 << 1$. The expression for the dispersion relation of the two low-energy bands is $E = \pm[\varepsilon_c^2 + t_1^2 + t_2^2 + 2t_1t_2\,\cos(k)]^{1/2}$. We note that the above expression resembles the band dispersion of a massive SSH chain with a complex mass term $\pm\varepsilon_c$. Moreover, through an appropriate choice of the momentum-dependent on-site potential ($\varepsilon_c = i\sqrt{\gamma^2 + 2i\gamma\,\sin k}$), one can simply map it to a nonreciprocal SSH model that features rich nonequilibrium topological phases and interesting many-body physics [63]. It is important to note that this decimation scheme is not a unique choice for mapping the five-site system to an identical two-level lattice. To establish this, we have alternatively eliminated all the doubly coordinated sites B, C, and D, resulting in an equivalent two-level ladder system consisting of only the originally triply coordinated A and E sites. Similar to the previous case, the decimated ladder network can be decoupled into a massive SSH chain where alternating sites have the on-site energies $+\varepsilon_c$ and $-\varepsilon_c$, and an array of isolated lattice sites with locally pinned eigenfunctions (see Appendix K for a detailed analysis). Therefore, the decimation scheme validates our hypothesis—in the low-energy limit, any quasi-one-dimensional bipartite non-Hermitian system exhibiting a flat band can be decoupled into a non-Hermitian SSH chain and periodically arranged isolated sites. The non-Hermitian SSH chain accounts for the band topology of the original lattice model, while the chain of isolated atoms manifests as a flat band and CLS. We have further verified the above hypothesis for other non-Hermitian lattice systems with flat bands, namely, stub and diamond lattices (see Appendix J for detailed analysis).

V. ANALYSIS OF HIGHER-ORDER TOPOLOGICAL INSULATING PHASES THROUGH THE LENS OF REAL-SPACE DECIMATION SCHEME

In this section, we comprehensively analyze the topological characteristics exhibited by second-order topological insulators (SOTIs) through the lens of the decimation scheme. Specifically, we focus on the celebrated Benalcazar–Bernevig–Hughes (BBH) model [64,65] and delve into the SOTI phase through its decimated rendition [see Fig. 7(a)]. The BBH model is formulated based on a four-band Bloch Hamiltonian,

$$\begin{aligned} H_{\mathrm{BBH}}(k) = {} & [t_1 + t_2\cos k_x]\tau_x\sigma_0 - t_2\sin k_x\tau_y\sigma_z \\ & - [t_1 + t_2\cos k_x]\tau_y\sigma_y - t_2\sin k_y\tau_y\sigma_x, \end{aligned} \tag{22}$$

where the Pauli matrices τ and σ act on distinct pseudospin/orbital degrees of freedom. Here, t_1 and t_2 denote the intra- and intercell hopping amplitudes, respectively. The model admits time-reversal symmetry (TRS), charge conjugation, chiral symmetry, and mirror symmetry along the x and y directions. Notably, the model showcases corner modes indicative of a second-order topological phase, as evident from Fig. 7, where four zero-energy eigenvalues ($E = 0$) are discernible.

To delineate the topological region within the parameter space of the Hamiltonian, we compare the eigenvalue spectra of the BBH model Hamiltonian and its decimated version under OBC as a function of the intracell hopping amplitude t_1 in Fig. 7(b). The comparison resembles striking correspondence harbouring localized zero-energy corner modes when the inter-cell hopping amplitude t_2 dominates over the intra-cell hopping, i.e., $|t_2/t_1| > 1$. Furthermore, the localized nature of these corner modes can be captured by computing the density of states of the decimated model in the nontrivial phase, as shown in Fig. 7(c), which shows robust localized states at $E = 0$ for $|t_2/t_1| > 1$.

VI. ANALYSIS OF HETEROSYSTEM INTERFACE CONSISTING OF HERMITIAN AND NON-HERMITIAN SSH CHAINS THROUGH REAL SPACE DECIMATION SCHEME

In this section, we consider a heterosystem interface consisting of Hermitian and non-Hermitian SSH chains [1], to test the generality and robustness of our formalism in understanding the topology of an interface system. The non-Hermitian SSH domain is represented by a top half circle with lattice sites in green and blue, while a bottom half circle with sites in red and yellow hues signifies the Hermitian region (see Fig. 8). The nearest-neighbor-hopping parameters for the non-Hermitian SSH chain are characterized by $t_1 \pm \gamma$ and t_2, whereas for the Hermitian part, they are denoted as t_1' and t_2'. We employ our decimation scheme to integrate a large number of degrees of freedom and decimate it to a smaller system, resulting in identical topological features.

For our numerical simulations we choose $t_2 = 1.0$, $\gamma = 1.5$, $t_2' = 0.5$, and $N = 18$ unit cells in both chains. Notably, the spectrum in the Hermitian SSH chain exhibits distinct features, being (b) gapped and (c) gapless as a function of t_1' (see Fig. 8). In this case, we have decimated all the bulk sites of the Hermitian and non-Hermitian SSH chains to obtain a renormalized lattice made of two pairs of interface sites only with energy dependent on-site and hopping matrices. The spectrum of the complete interface system is reliably reproduced using the decimation scheme.

VII. SUMMARY AND OUTLOOK

In conclusion, we have demonstrated the utility of the real-space decimation scheme in elucidating various aspects

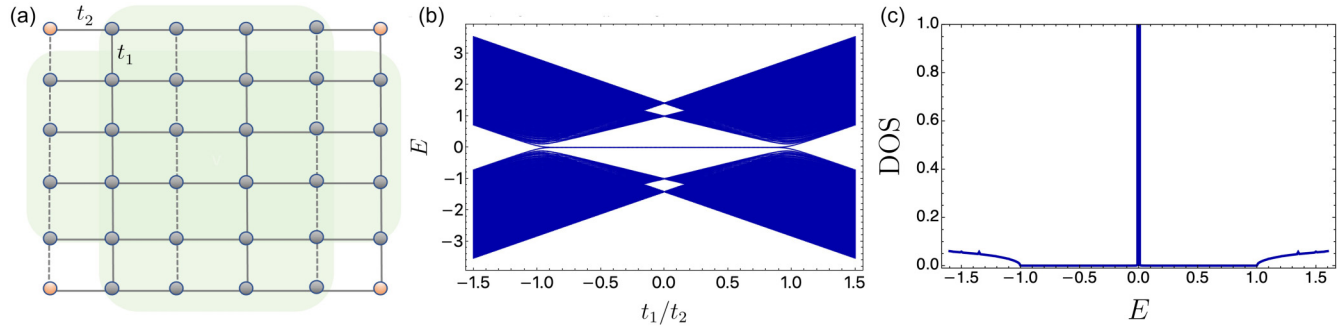

FIG. 7. Analysis of higher (second)-order topological phases through decimation scheme. (a) Schematic illustration of the BBH lattice model, with the unit cell consisting of four pseudo-spin/orbital degrees of freedom. The intracell (intercell) hopping is denoted by $t_1(t_2)$. Dashed lines indicate a negative hopping value. We have considered a 40×40 (here, 3×3 is shown for convenience), i.e., 6400 site BBH lattice in real space under open boundary conditions. Using the decimation scheme, we have eliminated all the internal atoms except for the four corner sites, as highlighted in green. (b) Similar to the original lattice, the decimated lattice gives rise to the topologically protected zero-energy corner modes in the nontrivial topological phase $|t_1/t_2| < 1$. (c) The appearance of the zero-energy corner modes has also been shown in the density of states spectra of the decimated model. Here we used the parameters $t_1 = 1.0$ and $t_2 = 2.0$.

of non-Hermitian spectral topology and emergent flat-band physics. Obtaining the band spectra of a non-Hermitian system is not an inherent advantage of this method, as these spectra can also be derived from the original Hamiltonian. However, the decimated model essentially offers several significant advantages, as highlighted earlier, to deal with the complex multiband non-Hermitian systems. For example, our study showcases the versatility of the decimation scheme, revealing not only an exact transformation reproducing the original system's band dispersion but also uncovering

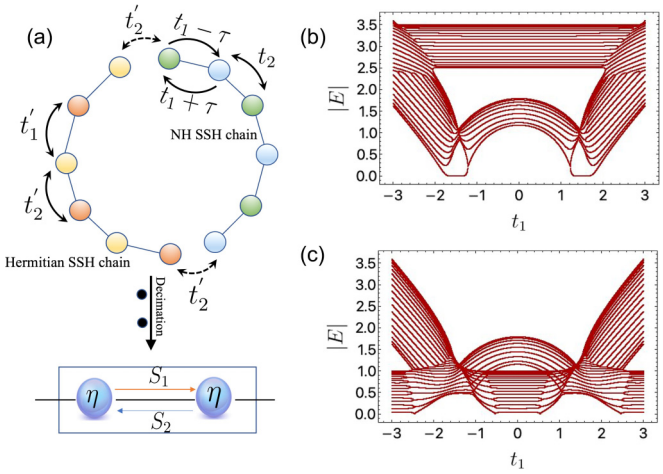

FIG. 8. Analysis of heterosystem interface through decimation scheme. (a) Schematic of interface system consisting of the Hermitian and non-Hermitian SSH chains. The coupling between them is t_2'. We reduce the system to a two-level problem with renormalized energy-dependent parameters (η, S_1, and S_2) in order to study the spectral topology. (b) For the Hermitian chain with a large gap ($t_1' = 3.0$), the zero mode of the non-Hermitian chain cannot leak into the Hermitian chain. (c) For a sufficiently small gap and finally when it is gapless ($t_1' = 0.5$), the zero-energy mode tends to tunnel through the Hermitian chain, and the zero-energy band starts to deviate from the EPs of the open system. We have chosen $t_2 = 1.0$, $\gamma = 1.5$, $t_2' = 0.5$, and $N = 18$ unit cells in both chains.

underlying physics governing various Hamiltonian features. Specifically, we show that the rich phase diagram of our four-level system, particularly the parameter-driven topological phase transitions, is underpinned by a simple SSH model, as evident from the decimation strategy. Hence, our demonstration underscores the potency of the decimation scheme in delving into the fundamental physics of seemingly simple non-Hermitian Hamiltonians, which are otherwise challenging to analyze. Additionally, the decimation approach facilitates deriving the analytical form of the dispersion relation, faithfully replicating the original Hamiltonian's intricate band structure. In particular, our systematic approach efficiently characterizes non-Hermitian phases and their transitions in complex multiband systems. Moreover, given the formidable challenge of constructing a GBZ for multiband non-Hermitian systems, our decimated two-level system offers an efficient solution pathway for this crucial task. Furthermore, we employ our formalism to study the skin mode physics, van Hove singularities using GBZ formulation and transmittance properties in disordered/defect-induced non-Hermitian chains. With the characteristic polynomial from the decimated Hamiltonian, we can leverage diverse analytical frameworks like Newton polygons and tropical geometry to delve into inherent properties such as higher-order EPs. Our approach has also shed light on CLSs in non-Hermitian systems, suggesting a hypothesis that quasi-one-dimensional non-Hermitian systems with flat bands can be decoupled into a non-Hermitian SSH chain and periodically arranged isolated sites. We elegantly showcase the adaptability of the real-space decimation method across a spectrum of models, spanning from higher-order topological insulators to the intricate interfaces between Hermitian and non-Hermitian systems, as well as systems featuring long-range hopping dynamics. Through our exploration, we unveil that employing Green's function formalism to compute the density of states in extensive systems with long-range hopping renders the decimation technique remarkably more computationally economical compared to utilizing the original Hamiltonian, owing to the considerably diminished size of the renormalized Hamiltonian. Similarly, the decimation strategy emerges

as a commendably efficient computational tool when evaluating transport properties such as transmittance. Hence, the decimation scheme stands as an exact transformation, offering significant advantages in elucidating the nuanced physics behind a plethora of intriguing and distinctive properties inherent to both Hermitian and non-Hermitian systems through analytical descriptions. We note that, in a very recent paper, the notion of biorthogonal polarization has been used to characterize the nontrivial topology of these systems [66].

We note that, in Ref. [67], the author presented a novel approach grounded in interface states across a broad spectrum of Hermitian and non-Hermitian models. This approach unveils a realm of interface physics governed by the dynamic interplay of microscopic interface parameters. The characteristics of the interface state intricately tie into the fixed-point topology of this dynamic flow. In contrast, our real-space decimation scheme provides a generalized approach to treat non-Hermitian complex multiband systems. While we have illustrated the decimation scheme for one-dimensional non-Hermitian problems, we envisage that it should be possible to generalize this to higher-dimensional cases, including the study of dislocation-induced skin and antiskin effects in two dimensions [68–71]. Since our approach allows treating the disorder in an efficient way, we also expect our analytical approach to be useful in studying the scale invariance and flat-band physics in non-Hermitian fractal networks [72,73]. It may also be interesting to employ our approach to use the renormalization flow equations to characterize critical phenomena and non-Hermitian phase transitions [74–77]. Our paper, bridging the realms of real-space renormalization schemes and non-Hermitian phenomena, is particularly timely given the surge of interest in non-Hermitian systems. We hope that our framework enables further work in this arena.

ACKNOWLEDGMENTS

A. Banerjee and R.S. are supported by the Prime Minister's Research Fellowship (PMRF). A. Bandyopadhyay acknowledges financial support IoE postdoctoral fellowship. A.N. acknowledges support from DST MATRICS Grant (No. MTR/2023/000021).

APPENDIX A: ANTI *PT*-SYMMETRIC SSH MODEL

In this Appendix, we consider the special case of our model with $\tau = 0$, leading to the anti-parity-time (APT) symmetric non-Hermitian SSH model introduced by Wu *et al.* [34]. The system features a four-band model with an even number of gain and loss pairs with intact inversion symmetry, unlike the PT-symmetric model. Before we proceed to the topological characterization of the model through the decimation scheme, we briefly discuss the salient features of the system. Interestingly, in this model, the spectral topology of the system can be controllably tuned by non-Hermitian coupling and non-Hermiticity coefficient, γ. The Bloch Hamiltonian of the system reads

$$H_k = \begin{pmatrix} i\gamma & t_1 & 0 & t_2 e^{-ik} \\ t_1 & -i\gamma & t_2 & 0 \\ 0 & t_2 & -i\gamma & t_1 \\ t_2 e^{ik} & 0 & t_1 & i\gamma \end{pmatrix}. \tag{A1}$$

The Hamiltonian describes a one-dimensional lattice with hopping strengths t_1 and t_2. Furthermore, we introduce inversion-symmetric gain-loss pairs into the four-site unit cell, which incorporates APT in the system. The APT is defined by $PTH_k(PT)^{-1} = -H_k$, where $P = i\sigma_x \otimes \sigma_y$ and $T = K$ is the complex conjugation operation. Additionally, the system also admits TRS†, PHS†, and chiral symmetries [6]. The model corresponds to BDI† symmetry class in the 38-fold topological classification of non-Hermitian systems. Interestingly, the topological phase transitions of the system can captured by a gap closing of real energy [6]. The model exhibits an interesting phase diagram and exhibits topological phase transitions from trivial phase to nontrivial topological phase with a pair of degenerated edge modes with net gain via exceptional points as a function of non-Hermiticity co-efficient. The system could be potentially useful for tunable topological lasing because of the positive gain rate of edge modes in the nontrivial regime [34].

APPENDIX B: DECIMATION SCHEME TO REVEAL THE GEOMETRIC PICTURE OF BAND TOPOLOGY

Next, we employ our formalism to decimate the four-band model to an effective two-band model with renormalized energy-dependent coupling, and gain and loss. We show that this effective two-band model can mimic the original model and capture all the essential physics of the system, as well as translate the known phase diagram with topological phase transitions, as discussed in the main text. The formalism is based on the finite difference method, which we illustrated in the formalism section.

We consider a chain of atoms and use the real-space decimation method to integrate out specific subsets of atomic sites. For instance, we integrate out two atoms out of four atoms in the four-site unit cell. The Schröedinger equation can be discretized and written in terms of a difference equation

$$(E - \epsilon_i)\phi_i = \sum_j t_{ij}\phi_j, \tag{B1}$$

where, E, ϵ_i, t_{ij}, and ϕ_i are the energy, on-site potential at the ith site, hopping integral between ith and jth site, and probability amplitude at the ith site, respectively. Here, we only consider the nearest-neighbor-hopping term. We can write down the difference equations using Eq. (B1) for the Hamiltonian as follows:

$$\begin{aligned} (E - i\gamma)\phi_a &= t_1\phi_b + t_2\phi'_d, \\ (E + i\gamma)\phi_b &= t_1\phi_a + t_2\phi_c, \\ (E + i\gamma)\phi_c &= t_2\phi_b + t_1\phi_d, \\ (E - i\gamma)\phi_d &= t_1\phi_c + t_2\phi''_a. \end{aligned} \tag{B2}$$

The primed parameters [X' (X'')] indicate the atoms in the adjacent right (left) unit cell. We have judiciously simplified Eq. (B2) to integrate out b and c sites from the lattice [see Fig. 2(a) in the main text], obtaining

$$[E - \epsilon'']\phi_a = \sigma\phi_d + t_2\phi'_d, \tag{B3}$$

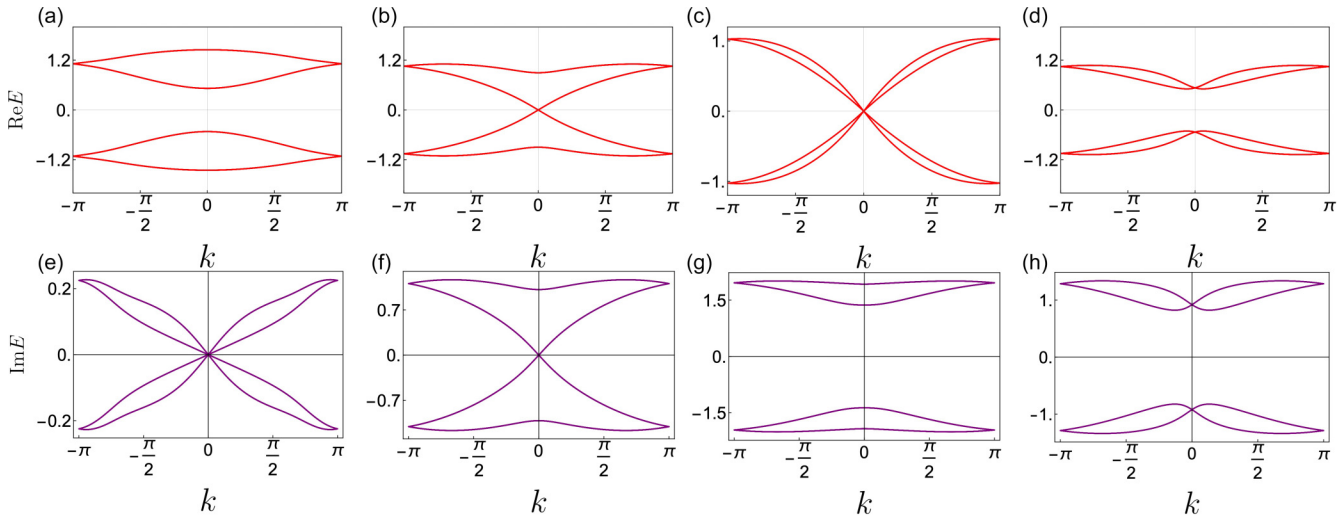

FIG. 9. Band dispersion of nonreciprocal SSH model in the presence of *APT* staggered imaginary potential. The four phases, corresponding to the phase diagram in the main text (see Fig. 2), exhibit gapless spectra as well as distinct real and imaginary line gaps. The transitions among the phases are characterized by exceptional physics with the absolute energy gap closing. We set $\gamma = 0.11$, $\tau = 0.13$ for (a) and (e), $\gamma = 0.27$, $\tau = 0.82$ for (b) and (f), $\gamma = 0.63$, $\tau = 1.83$ for (c) and (g), $\gamma = 1.22$, $\tau = 0.29$ for (d) and (h).

and

$$[E - \epsilon'']\phi_d = \sigma\phi_a + t_2\phi'_a, \tag{B4}$$

where $\epsilon'' = i\gamma + \frac{t_1^2}{E-\epsilon'}$, $\epsilon' = \frac{t_2^2}{E+i\gamma} - i\gamma$, and $\sigma = \frac{t_1{}^2 t_2}{(E+i\gamma)(E-\epsilon')}$. Thus, we get an effective two-band model with energy-dependent renormalized coupling and gain and loss terms. The Hamiltonian has the form

$$\begin{pmatrix} \epsilon'' & \sigma + t_2 e^{-ika} \\ \sigma + t_2 e^{ika} & \epsilon'' \end{pmatrix} \tag{B5}$$

It is interesting to note that the dispersion mimics the original four-site model throughout the parameter space (see Fig. 9).

Next, we consider the low-energy limit of the model $E \to 0$ and show that one can map the model to an effective SSH model. The topological phase transition and associated geometric interpretation of spectral properties of the original model would entirely captured by this effective SSH model in the same parameter regime as that of the original model. We now study the topological phase transitions of the system driven by the non-Hermiticity factor γ in terms of the orbital character of the bands. We write the creation operators for two bands as $c^\dagger_{k\alpha} = \frac{1}{\sqrt{2}}(c^\dagger_{kA} + c^\dagger_{kB})$ and $c^\dagger_{k\beta} = \frac{1}{\sqrt{2}}(c^\dagger_{kA} - c^\dagger_{kB})$. Next, decomposing the band wavefunctions ($n = 0, 1$) into the bonding and antibonding contributions in terms of creation operators, $c^\dagger_{nk} = \psi^n_{\alpha k} c^\dagger_{k\alpha} + \psi^n_{\beta k} c^\dagger_{k\beta}$, we plot $|\psi^n_{\alpha k}|^2$ for both the bands. These show the characteristic twist of the bands in the nontrivial (topological) region ($\gamma^2 < t_1^2 - t_2^2$) revealing the orbital nature of the bands [see Figs. 2(e) and 2(f) in the main text]. While in the trivial region ($\gamma^2 > t_1^2 - t_2^2$), there is no mixing in the orbital character of the bands. The orbital nature of these two regimes can be distinguished by electric polarization, which is a measurable quantity [78].

APPENDIX C: SPECTRAL TOPOLOGY OF THE FOUR-SITE MODEL

In this Appendix, we present a comprehensive analysis of the phase diagram, elucidating the unique spectral topology through the non-Hermitian winding number. Additionally, we explore the relationship between the topological winding number and the chiral modes in the system. The phase diagram is divided into four regions (see Fig. 2 in the main text).

(I) The spectrum, when plotted in the complex plane (Re[E], Im[E]) comprises of two spectral lobes separated in real energy by a line gap [see Fig. 10(a)]. (II) The spectral topology is that of a single loop in the complex plane [see Fig. 10(b)]. (III) The complex spectrum has a two-lobe structure with the lobes vertically displaced along the imaginary axis [see Fig. 10(c)]. We obtained the fourth phase (IV) with four lobes shifted in real and imaginary directions [see Fig. 10(d)]. These four phases and their transitions are related to distinct changes in the Fermi surface topology, namely, Lifshitz transitions. The band dispersion corresponding to these four phases is shown in Fig. 9. The spectral topology can be characterized by the non-Hermitian winding number, w, which is expressed as [8,79]

$$w = \int_{-\pi}^{\pi} \partial_k(\log(\det[H_d(k) - E_B]))dk/2\pi i, \tag{C1}$$

where E_B is the chosen base energy. The four regions are characterized by winding numbers (1, 1/2, 0, 0), respectively. Interestingly, these winding numbers have a one-to-one correspondence with the nondecaying chiral modes [80,81]. The connection between the winding number and chiral modes can be established as follows:

$$\omega = \frac{1}{2}\sum_{n\alpha} \text{sign}[\text{Im}(E_n(k_{n\alpha}))]\text{sign}[\partial_k[\text{Re}(E_n(k_{n\alpha}))]], \tag{C2}$$

where $k_{n\alpha} : \text{Re}(E_n(k_{n\alpha})) = 0$ represents the set of wavevectors where the real part of the energy vanishes, and α labels

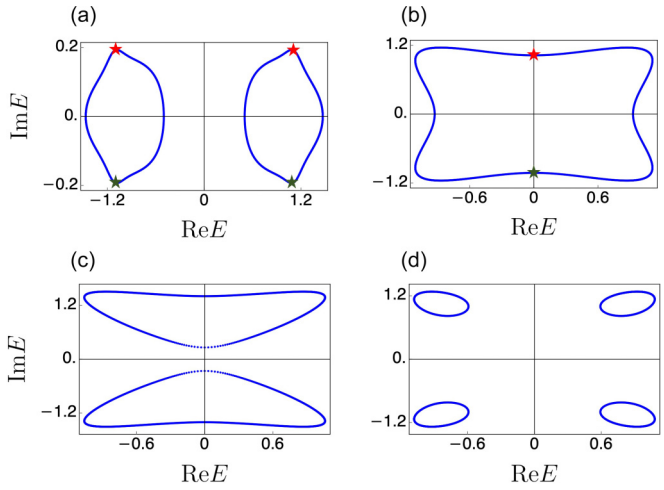

FIG. 10. Various phases of nonreciprocal SSH model in the presence of *APT* staggered imaginary potential. The four phases corresponding to the phase diagram in the main text (see Fig. 2) exhibit distinct spectral topology consisting of point and line gaps. The phase transitions are characterized by Lifshitz transitions. The phase transition lines define the locus of second-order exceptional points. The chiral modes are indicated in red and green. We consider the same parameters chosen in Fig. 9 for the four phases.

the number of connected points in the spectrum with such properties. Here n denotes the band index. Therefore, the topological winding number of the complex spectrum signifies the count of chiral modes where $\mathrm{Re}(E_n(k_{n\alpha})) = 0$. The term $\mathrm{sign}[\mathrm{Im}(E_n(k_{n\alpha}))]$ picks up the sign of the imaginary parts of the zero modes (modes with zero real parts), effectively quantifying the dynamically growing or decaying modes. This suggests that only one of the chiral modes with positive imaginary parts dynamically survives at long time. The chiral modes are designated by red and green dots in Fig. 10.

APPENDIX D: CHARACTERIZATION OF EXCEPTIONAL POINTS THROUGH NEWTON POLYGONS AND TROPICAL GEOMETRY

As discussed in the preceding Appendix, the phase transition lines dividing the different phases signify the locus of exceptional points enabling non-Hermitian phase transitions. We characterize the exceptional points from our downfolded two-band model using algebraic topology, specifically with the help of Newton polygons and tropical geometry. We note that this algebraic-geometric framework we discuss below can characterize the exceptional points even in the presence of energy-dependent coupling parameters in the decimated model. Interestingly, the algebraic-geometric information is encoded in the characteristics polynomial of the decimated model. The characteristic equation under low energy expansion around $k = 0$ reads

$$E_1^2 - \left(\sqrt{3}E_1 + 2iE_1^2 - i\right)k + \left(0.5 + i\frac{\sqrt{3}}{2}E_1 - E_1^2\right)k^2 = 0. \tag{D1}$$

Next, we individually discuss Newton's polygon method and tropical geometry formalism, illustrating their exceptional characterisation.

1. Newton polygon method

Consider the characteristic equation of the form $p(\omega, \epsilon) = \det(H - \omega\mathbb{I}) = 0$, and express it as a polynomial in terms of ω and ϵ as follows: $p(\omega, \epsilon) = \sum_{m,n} a_{mn}(t_1, t_2, \ldots)\omega^m\epsilon^n$. Each term in this polynomial can be represented as a point (m, n) in $\mathbb{R}^2$. The collection of these points forms a set, and the smallest convex shape that encloses all plotted points is known as the Newton polygon [42].

To determine the lowest-order dependence of ω on ϵ, we need to select a line segment from the Newton polygon in a way that all plotted points are either on, above, or to the right of it. The negative slope of this line segment will provide us with the desired information about the lowest order dependence of ω on ϵ characterising the exceptional point. For our model, the Newton polygon and the characterization of the exceptional point are shown in Fig. 2(g) in the main text.

2. Tropical geometry formalism

The tropical geometric approach is based on evaluating the characteristic polynomial using a concept called "valuation" [41]. The valuation is defined as follows:

(i) The valuation of a is ∞ if and only if $a = 0$.

(ii) The valuation of the product of two elements, ab, is the sum of their individual valuations: $\mathrm{val}(ab) = \mathrm{val}(a) + \mathrm{val}(b)$.

(iii) The valuation of the sum of two elements, $a + b$, is greater than or equal to the minimum of their individual valuations: $\mathrm{val}(a + b) \geqslant \min\{\mathrm{val}(a), \mathrm{val}(b)\}$ for all $a, b \in \mathbb{K}$, where $\mathbb{K}$ is a complex field.

This framework mainly deals with the field of the Puiseux series having coefficients in the complex numbers $\mathbb{C}$. This field possesses a natural valuation, which considers the lowest exponent appearing in the expansion of a nonzero Puiseux series. For instance, $\mathrm{val}(t^3 - 2t^2 + 3) = \min\{\mathrm{val}(t^3), \mathrm{val}(-2t^2), \mathrm{val}(3)\} = \min\{3, 2, 0\} = 0$.

At its core, tropical geometry provides a method to compute the valuations of nonzero roots of a nonzero polynomial $p \in \mathbb{K}[\lambda]$ in terms of the valuations of its coefficients. More precisely, given the nonzero polynomial $p = \sum_{i=0}^{d} a_i\lambda^i \in \mathbb{K}[\lambda]$, its tropicalization $\mathrm{trop}(p) : \mathbb{R} \to \mathbb{R}$ is defined as $\mathrm{trop}(p)(\omega) = \min_i \mathrm{val}(a_i) + i \cdot \omega$. A real number ω_0 is termed a "tropical root" of $\mathrm{trop}(p)$ if the minimum defining $\mathrm{trop}(p)(\omega_0)$ is achieved by at least two distinct terms $\mathrm{val}(a_j) + j \cdot \omega_0$ and $\mathrm{val}(a_k) + k \cdot \omega_0$ for $j \neq k$. In other words, the tropical roots of $\mathrm{trop}(p)$ correspond precisely to the real numbers where $\mathrm{trop}(p)$ is nondifferentiable, forming the "bend locus" of $\mathrm{trop}(p)$. The tropical root defines the order of exceptional points, thus characterizing exceptional physics.

For our case, the tropicalization corresponding to Eq. (D1) leads to $\mathrm{trop}(p(E, k)) = \{2E, 2E + 2, 2E + 1, E + 2, E + 1, 2, 1\}$. The bend locus is shown in Fig. 2(h) in the main text.

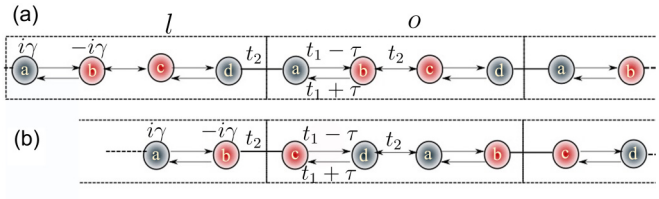

FIG. 11. Comparison between different decimation schemes for four band model. (a) Decimation scheme for eliminating sites a and d. (b) Illustration of the equivalence between two decimation schemes (decimation scheme for b and c and a and d) with relative sign change in γ. These schemes are mapped by shifting the unit cells by half the cell size.

APPENDIX E: COMPARISON BETWEEN DIFFERENT DECIMATION SCHEMES FOR FOUR-BAND MODEL

The present decimation model is an exact formalism that does not lose any information of the original model. In other words, the energy band dispersion remains invariant under this exact transformation, which gives rise to exactly the same real and imaginary band structure. The decimation scheme essentially rewrites the new effective on-site energies and hopping parameters of the downfolded system in terms of all the on-site and hopping parameters of the original lattice model, keeping the dispersion relation invariant. Naturally, the choice of degrees of freedom to be decimated is not very stringent. For example, as no spectral information of the original Hamiltonian is lost during the transformation, decimating B and C sites is one of the many choices to obtain a reduced renormalized lattice. Please note that for the model given in Eq. (10), the renormalized two-level system can also be achieved by equivalent decimation routes, i.e., decimating {a and b}, or, say, {a and d} lattice sites. We want to emphasize that these transformations yield the same characteristic equation, which provides exactly the same complex energy dispersion plots. Therefore, one can choose any of these similar paths to decimate the system to a low-level model without any ambiguity. We have added the decimation results, i.e., the renormalized hopping and on-site parameters for the above-mentioned decimation routes, to establish that the characteristic equation is invariant.

Let us consider the following scheme, which enables decimating d and a sites. We start with the difference equation for a and d sites (see the unit cell denoted by l and o in Fig. 11)

$$(E - i\gamma)\psi_a^o = t_2\psi_d^l + (t_1 - \tau)\psi_b^o, \tag{E1}$$

and

$$(E - i\gamma)\psi_d^l = t_2\psi_a^o + (t_1 + \tau)\psi_c^l. \tag{E2}$$

Next, we substitute Eq. (E2) into Eq. (E1) to obtain

$$(E - \epsilon')\psi_a^o = \frac{t_2(t_1 + \tau)}{E - i\gamma}\psi_c^l + (t_1 - \tau)\psi_b^o, \tag{E3}$$

and

$$(E - \epsilon')\psi_d^l = \frac{t_2(t_1 - \tau)}{E - i\gamma}\psi_b^o + (t_1 + \tau)\psi_c^l, \tag{E4}$$

where, $\epsilon' = i\gamma + \frac{t_2^2}{E - i\gamma}$.

Next, we write the difference equation for b and c using Eqs. (E3) and (E4),

$$(E - \epsilon'')\psi_b^o = \frac{t_2(t_1 + \tau)^2}{(E - i\gamma)(E - \epsilon')}\psi_c^l + t_2\psi_c^o, \tag{E5}$$

and

$$(E - \epsilon'')\psi_c^l = \frac{t_2(t_1 - \tau)^2}{(E - i\gamma)(E - \epsilon')}\psi_b^l + t_2\psi_b^l, \tag{E6}$$

where the renormalized on-site parameter $\epsilon'' = -i\gamma + \frac{t_1^2 - \tau^2}{E - \epsilon'}$ and the hopping between $b \to c$ and $c \to b$ are represented by $t_{b\to c} = \frac{t_2(t_1+\tau)^2}{(E-i\gamma)(E-\epsilon')}$ and $t_{c\to b} = \frac{t_2(t_1-\tau)^2}{(E-i\gamma)(E-\epsilon')}$.

The above expressions for the renormalized parameters are expected because of the transformation $c \leftrightarrow a$ and $d \leftrightarrow b$ under $\gamma \leftrightarrow -\gamma$ presented in the main text while decimating b and c sites. Please note that both decimation schemes lead to the same characteristic polynomials. Figure 11 demonstrates that shifting the unit cell by half its size directly maps to the decimation scheme for b and c, enabling the switching of the γ sign.

APPENDIX F: ANALYZING BBC USING TRANSFER MATRIX APPROACH

In this Appendix, we investigate the BBC via the transfer matrix approach. We consider the tight-binding chain under OBC with N unit cells. The Q1D Hamiltonian can be written as [47]

$$H = \sum_i (J_L c_i^\dagger c_{i+1} + M c_i^\dagger c_i + J_R^\dagger c_{i+1}^\dagger c_i). \tag{F1}$$

J_L and J_R denote the nearest-neighbor-hopping terms, while M is the on-site term. Note that a single-particle state can be expressed as $|1\rangle = \sum_{n=0}^{N} \psi_n c_n^\dagger |0\rangle$, with $|0\rangle$ being the vacuum state. Plugging this wavefunction in the Schröedinger equation $H(k)|\psi\rangle = \varepsilon|\psi\rangle$ results in

$$J|\psi_{n+1}\rangle + M|\psi_n\rangle + J^\dagger|\psi_{n-1}\rangle = \varepsilon|\psi_n\rangle, \tag{F2}$$

for $J_L = J_R^\dagger$. The hopping matrix can be written by using the singular value decomposition

$$J = V\Xi W^\dagger, \tag{F3}$$

where $\Xi = \mathrm{diag}\{\eta_1, \eta_2, \cdots \eta_r\}$ with η_i positive and real. V and W denote: $V = \{v_1, v_2, , v_r\}$, $W = \{w_1, w_2, , w_r\}$, which admit the relations $V^\dagger V = W^\dagger W = 1$, $V^\dagger W = 0$. r is the rank of matrix J. Rewriting Eq. (F2) in terms of the on-site Green's function $G = \frac{1}{\varepsilon - M}$, which eventually gives rise to

$$\psi_n = GJ\psi_{n+1} + GJ^\dagger\psi_{n-1}. \tag{F4}$$

To construct the transfer matrix, we use the substitutions $\alpha_n = V^\dagger\psi_n$ and $\beta_n = W^\dagger\psi_n$. We follow the prescription introduced by Kunst *et al.* [47] and multiply $V^\dagger$ and $W^\dagger$ to Eq. (F4), to obtain the following relation $\phi_{n+1} = \mathcal{T}\phi_n$; $\phi_n = (\beta_n, \alpha_{n-1})^T$. Here $\mathcal{T}$ is the transfer matrix given by

$$\mathcal{T} = \frac{1}{G_{vw}}\begin{pmatrix} \frac{1}{\eta} & -G_{ww} \\ G_{vv} & \eta(G_{vw}G_{wv} - G_{vv}G_{ww}) \end{pmatrix}. \tag{F5}$$

Next, we will calculate our system's transfer matrix using Eq. (F1) corresponding to the Bloch Hamiltonian. We

have $J = \begin{pmatrix} 0 & 0 \\ t_2 & 0 \end{pmatrix}$ and $M = \begin{pmatrix} \varepsilon & -2t_1\nu\tau + \nu(t_1^2+\tau^2) \\ 2t_1\nu\tau + \nu(t_1^2+\tau^2) & \varepsilon \end{pmatrix}$, where $\nu = \frac{t_2}{(E+i\gamma)(E-\epsilon')}$. The on-site Green's function can be written as

$$G = \frac{1}{(E-\varepsilon)^2 - \nu^2\left(t_1^2+\tau^2\right) + 4t_1^2\nu^2\tau} \begin{pmatrix} E-\varepsilon & -2t_1\nu\tau + \nu\left(t_1^2+\tau^2\right) \\ 2t_1\nu\tau + \nu\left(t_1^2+\tau^2\right) & E-\varepsilon \end{pmatrix}. \quad \text{(F6)}$$

The singular value decomposition of $J = V\,\Xi W^\dagger$ gives $V = \begin{pmatrix} 0 & 1 \\ 1 & 0 \end{pmatrix}$, $\Xi = \begin{pmatrix} t_2 & 0 \\ 0 & 0 \end{pmatrix}$ and $W = \begin{pmatrix} 1 & 0 \\ 0 & 1 \end{pmatrix}$. The trace of the transfer matrix in Eq. (F5) is obtained as $\det\mathcal{T} = \frac{\nu(t_1^2+\tau^2)+2t_1\nu\tau}{\nu(t_1^2+\tau^2)-2t_1\nu\tau}$. This immediately gives us

(i) $\tau \to 0 \Rightarrow \det\mathcal{T} = 1$ restores the BBC.

(ii) $\tau \neq 0 \Rightarrow \det\mathcal{T} \neq 1$ results in broken BBC and disparity in periodic and open spectra.

(iii) $t_1 = |\tau| \Rightarrow \det\mathcal{T} = 0$ leads to a higher order exceptional point in the OBC spectrum.

APPENDIX G: ANALYSIS OF SKIN EFFECT AND ZERO-ENERGY MODES

In this Appendix, we derive the condition given in Eq. (13) of the main text for the parameter β that governs the bulk states under OBC. We begin by considering the one-dimensional real-space tight-binding model with two orbitals, A and B, within a unit cell for the momentum-space Hamiltonian described in Eq. (11) of the main text. The real-space wavefunction is subject to the following constraints:

$$\begin{aligned} \Theta'\psi_{a,n} + t_2\psi_{a,n+1} + \varepsilon_n\psi_{b,n} &= E\psi_{b,n}, \\ \Theta\psi_{b,n} + t_2\psi_{b,n-1} + \varepsilon_n\psi_{a,n} &= E\psi_{a,n}. \end{aligned} \quad \text{(G1)}$$

The spatial periodicity enables us to take the following ansatz, $(\psi_{an}, \psi_{bn}) = \beta^n(\psi_a, \psi_b)$. We obtain

$$\begin{aligned} \Theta'\psi_a + t_2\beta\psi_a + (\varepsilon_n - E)\psi_b &= 0, \\ \Theta\psi_b + t_2\frac{1}{\beta}\psi_b + (\varepsilon_n - E)\psi_a &= 0. \end{aligned} \quad \text{(G2)}$$

This leads to the following condition

$$\beta^2 t_2\Theta + \beta\left\{\Theta\Theta' + t_2^2 - (\varepsilon_n - E)^2\right\} + t_2\Theta' = 0. \quad \text{(G3)}$$

The roots of the above equation satisfy the following condition, $\beta_1\beta_2 = \frac{\Theta'}{\Theta}$. It can be shown that the bulk states of a long chain require $|\beta_1| = |\beta_2|$. This immediately suggests that $|\beta| = |\beta_1| = |\beta_2| = \sqrt{|\Theta'/\Theta|}$. This condition $|\beta| < 1$ ($|\beta| > 1$) dictates that the bulk states are localized at the left (right) end of the chain.

We find the zero-energy mode condition considering the low energy approximation. Eq. (G3), in the $E \to \varepsilon_m$ limit becomes

$$\beta^2 t_2\Theta + \beta\left\{\Theta\Theta' + t_2^2\right\} + t_2\Theta' = 0. \quad \text{(G4)}$$

This quadratic equation in β gives rise to two roots $\beta = \frac{-\Theta'}{t_2}$ or $\frac{-t_2}{\Theta}$. We obtain solutions of the zero-energy modes with parametric dependence $t_2^2 = \Theta\Theta'$ by equating $|\beta| = \sqrt{|\Theta'/\Theta|} = \frac{-\Theta'}{t_2} = \frac{-t_2}{\Theta}$.

APPENDIX H: FORMULATION OF GENERALIZED BRILLOUIN ZONE

In this Appendix, we construct the generalized Brillouin zone (GBZ) formalism and explore the van Hove singularity in light of the saddle point coalescing in the GBZ. We start with Eq. (G2), which leads to the following condition:

$$(\Theta' + t_2\beta)(\Theta + t_2/\beta) = (E-\varepsilon)^2. \quad \text{(H1)}$$

Replacing Θ and Θ', we get

$$M(E,\beta) = f(\beta) - g(E) = 0, \quad \text{(H2)}$$

where $f(\beta) = (t_1+\tau)^2\frac{1}{\beta} + (t_1-\tau)^2\beta$ and $g(E) = [\frac{(E+i\gamma)^2-t_2^2}{t_2^2}]\{[E - i\gamma - \frac{(t_1\tau)(t_1+\tau)(E+i\gamma)}{(E+i\gamma)^2-t_2^2}]^2 - \frac{(t_1-\tau)^2(t_1+\tau)^2t_2^2}{[(E+i\gamma)^2-t_2^2]^2} - t_2^2\}$. One can consider the two solutions β and β' to have the same absolute values, $|\beta| = |\beta'|$. Then, we get $\beta' = \beta e^{i\theta}, \theta \in \mathbb{R}$. This enables us to write $f(\beta) - f(\beta e^{i\theta}) = 0$. Solving this equation, we obtain $\beta = \pm e^{-i\theta/2}$ with $\theta \in [0, 2\pi)$. This equation enables us to calculate β for any given value of $\theta \in [0, 2\pi)$. Subsequently, we derive a set of values of β that satisfy the condition $|\beta| = |\beta'|$. By judiciously choosing values of β and β' that meet this equality criterion, we can obtain the GBZ.

Subsequently, we determine the condition for saddle points within the GBZ as $\partial_\beta M(E,\beta) = 0$. Solving this condition yields $|\beta| = \pm\frac{t_1+\tau}{t_1-\tau}$. As a result, two saddle points coalesce at $t_1 = -\tau$, leading to the occurrence of a van Hove singularity in the density of states.

APPENDIX I: FORMULATION OF GBZ IN THE PRESENCE OF NEXT-NEAREST-NEIGHBOR HOPPING

We start with the Hamiltonian [see Eq. (10) in the main text], which features a four-band model having both nonreciprocal hopping and inversion symmetric imaginary potentials. To see the effect of the next-nearest-neighbor hopping on the GBZ formulation, we add a hopping of strength t_3 between the first and second sites of the adjacent unit cells (see Fig. 12). Next, we employ the decimation scheme to obtain a two-site model by integrating out the other two degrees of freedom. We have judiciously simplified Eq. (B1) (see the main text) to integrate out c and d sites from the unit cell, obtaining

$$[E - O_a]\phi_{a_2} = (t_1 - \tau)\phi_{b_2} + \alpha_1\phi_{b_1} + t_3\phi_{b_3}, \quad \text{(I1)}$$

and

$$[E - O_b]\phi_{b_1} = \alpha_2\phi_{a_2} + (t_1 + \tau)\phi_{a_1} + t_3\phi_{a_0}, \quad \text{(I2)}$$

where $O_a = i\gamma + \frac{t_2^2}{E-\epsilon_d}$, $O_b = -i\gamma + \frac{t_2^2}{E-\epsilon_c}$, $\epsilon_c = i\gamma + \frac{(t_1-\tau)(t_1+\tau)}{(E-i\gamma)}$, $\epsilon_d = i\gamma + \frac{(t_1-\tau)(t_1+\tau)}{(E+i\gamma)}$, $\alpha_1 = \frac{t_2^2(t_1+\tau)}{(E-\epsilon_d)(E+i\gamma)}$, and $\alpha_2 = \frac{t_2^2(t_1-\tau)}{(E-\epsilon_c)(E+i\gamma)}$. The decimated Hamiltonian with renormalized energy-dependent coupling reads

$$H_d = \begin{pmatrix} O_a & t_1 - \tau + \alpha_1 e^{-ika} + t_3 e^{ika} \\ t_1 + \tau + \alpha_2 e^{ika} + t_3 e^{-ika} & O_b \end{pmatrix}. \quad \text{(I3)}$$

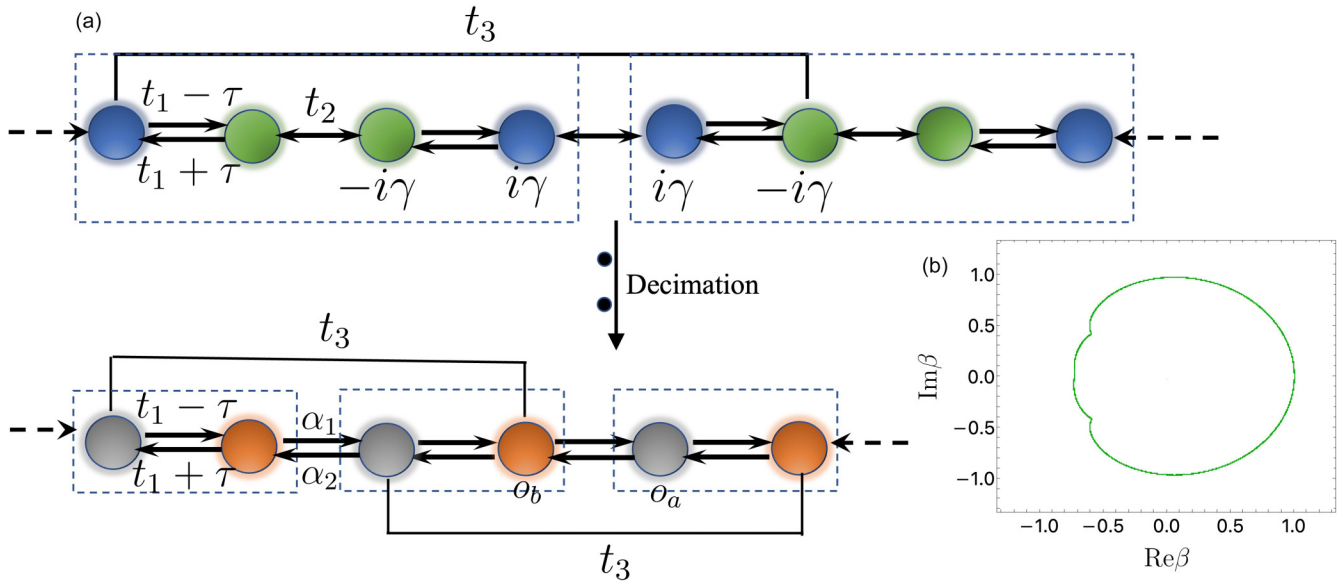

FIG. 12. GBZ formulation for model with next-nearest-neighbor hopping. (a) A schematic of the model with next-nearest-neighbor hopping and its decimation scheme illustrating the two-band model. We note that only one representative next-nearest-neighbor coupling t_3 is shown here. In the original next-nearest-neighbor model each A and B sites are coupled with each other in the adjacent cells. (b) The GBZ for the decimated model with parameters $t_1 = 1.0$, $t_2 = 1.0$, $\tau = 0.1$, $\gamma = 1$, and $t_3 = 1$. Note the noncircular shape of the GBZ.

Next, we write $M(E, \beta) = H_d(e^{ik} \to \beta) - E\mathcal{I}$ as a decoupled form for further analysis, $M(E, \beta) = f(\beta, E) - g(E) = 0$. As we discussed in the earlier Appendix, the condition $M(E, \beta) - M(E, \beta e^{i\theta}) = 0$ gives the GBZ for any given values of $\theta \in [0, 2\pi)$ satisfying the following condition on the roots of β: $|\beta_1| < |\beta_2| = |\beta_3| < |\beta_4|$. This results in the GBZ with two cusps (see Fig. 12). We note that $t_3 \to 0$ leads to the previous criterion ($\beta = \sqrt{|(t_1+\tau)^2/(t_1-\tau)^2|}$) with vanishing next-nearest-neighbor hopping (as presented in the main text).

APPENDIX J: DECOUPLING OF FLAT BAND AND SSH CHAIN IN THREE-SITE DIAMOND AND STUB LATTICES THROUGH THE DECIMATION SCHEME

We start with a generalized one-dimensional trimer model with bipartite sublattice symmetry, where the system decouples into an SSH chain along with a localized flat band. Eventually, we consider the model with non-Hermitian coupling strength leading to the formation of an Aharonov-Bohm cage with a net magnetic flux [17]. The Bloch Hamiltonian of the system reads

$$H_k = \begin{pmatrix} 0 & \kappa_1 + \kappa_2 e^{ik} & 0 \\ \kappa_1 + \kappa_2 e^{-ik} & \Delta & \kappa_3 + \kappa_4 e^{-ik} \\ 0 & \kappa_3 + \kappa_4 e^{ik} & 0 \end{pmatrix}, \tag{J1}$$

where κ_j are complex coupling terms and Δ denotes the detuning of the central sites [see Fig. 2(a) of main text]. As we discussed in the main text, we employ our decimation scheme and write down the tight-binding analog of the Schrödinger

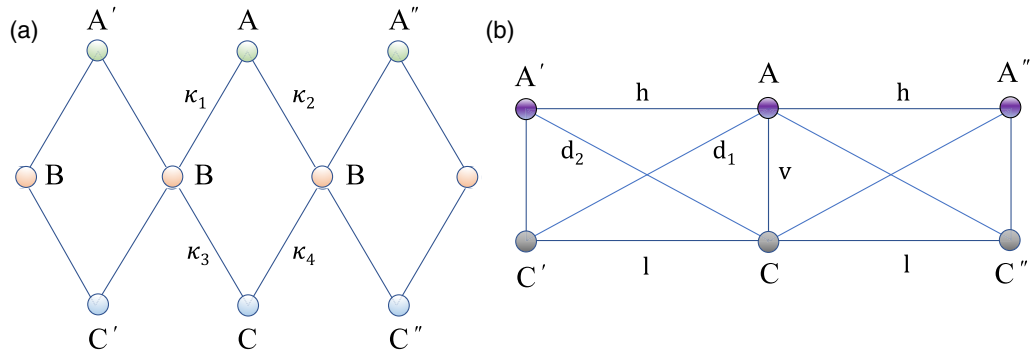

FIG. 13. Illustration of decoupling into SSH chain and flat band through a three-site trimer model. (a) Schematic of the trimer lattice consisting of A, B, and C sites with bipartite sublattice symmetry featuring a flat band at zero energy. The on-site potential of A, B, and C are Δ_1, Δ_2, and Δ_3, respectively. κ_i represents the non-Hermitian coupling. (b) We use the decimation scheme to eliminate the C site and obtain an effective two-level system. The effective model can characterize the flat-band physics and the decoupled SSH spectra. Furthermore, we modify the coupling to get the non-Hermitian stub and diamond lattices, which feature exceptional physics and flat bands.

equation as follows:

$$\begin{aligned}
(E-\Delta_1)\psi_A &= \kappa_1\psi_B + \kappa_2\psi_B',\\
(E-\Delta_2)\psi_B &= \kappa_1\psi_A + \kappa_3\psi_C + \kappa_2\psi_A' + \kappa_4\psi_C',\\
(E-\Delta_3)\psi_C &= \kappa_4\psi_B' + \kappa_3\psi_B,\\
(E-\Delta_4)\psi_B' &= \kappa_2\psi_A + +\kappa_1\psi_A'' + \kappa_3\psi_c'' + \kappa_4\psi_c. \qquad \text{(J2)}
\end{aligned}$$

Note that we choose $\Delta_1 = \Delta_3 = 0$ and $\Delta_2 = \Delta_4 = \Delta$. We integrate out the central site from the lattice to obtain the following coupled equations:

$$\begin{aligned}
\left(E - \frac{\kappa_1^2+\kappa_2^2}{E-\Delta}\right)\psi_A &= \frac{\kappa_1\kappa_3+\kappa_2\kappa_4}{E-\Delta}\psi_C + \frac{\kappa_1\kappa_2}{E-\Delta}\psi_A'\\
&\quad + \frac{\kappa_1\kappa_4}{E-\Delta}\psi_C' + \frac{\kappa_2\kappa_1}{E-\Delta}\psi_A''\\
&\quad + \frac{\kappa_2\kappa_3}{E-\Delta}\psi_C'',\\
\left(E - \frac{\kappa_3^2+\kappa_4^2}{E-\Delta}\right)\psi_C &= \frac{\kappa_2\kappa_4+\kappa_1\kappa_3}{E-\Delta}\psi_C + \frac{\kappa_1\kappa_4}{E-\Delta}\psi_A''\\
&\quad + \frac{\kappa_3\kappa_4}{E-\Delta}\psi_C'' + \frac{\kappa_2\kappa_3}{E-\Delta}\psi_A' + \frac{\kappa_3\kappa_4}{E-\Delta}\psi_C'.
\end{aligned}$$

The above-coupled equation leads to the two-level Hamiltonian

$$H_k = \begin{pmatrix} \epsilon_1 + 2h\cos k & v + d_1e^{-ik} + d_2e^{ik} \\ v + d_1e^{ik} + d_2e^{-ik} & \epsilon_2 + 2l\cos k \end{pmatrix}, \qquad \text{(J3)}$$

with the following parameters $h = \frac{\kappa_1\kappa_2}{E-\Delta}$, $l = \frac{\kappa_3\kappa_4}{E-\Delta}$, $v = \frac{\kappa_1\kappa_3+\kappa_2\kappa_4}{E-\Delta}$, $d_1 = \frac{\kappa_1\kappa_4}{E-\Delta}$, $d_2 = \frac{\kappa_2\kappa_3}{E-\Delta}$, $\epsilon_1 = \frac{\kappa_1^2+\kappa_2^2}{E-\Delta}$ and $\epsilon_2 = \Delta + \frac{\kappa_3^2+\kappa_4^2}{E-\Delta}$. The eigenspectra $E = 0, \frac{1}{2}(\Delta \pm 2\sqrt{2}\sqrt{\Delta^2/8 + \kappa_1^2 + \kappa_2^2 + 2\kappa_1\kappa_2\cos k})$ feature a massive SSH dispersion along with a nondispersive flat band for $\kappa_1 = \kappa_3$ and $\kappa_2 = \kappa_4$. Next, we discuss two kinds of non-Hermitian coupling terms leading to diamond and stub lattices, as discussed by Leykam *et al.* [17].

We consider a non-Hermitian diamond lattice with two legs consisting of opposite non-Hermitian coupling strengths, $\kappa_1 = C + i\gamma$, $\kappa_2 = \alpha\kappa_1$ ($\alpha \in \mathbb{R}$), $\kappa_3 = \kappa_1^*$, and $\kappa_4 = \kappa_2^*$. Consequently, the upper (lower) leg accumulates a phase θ ($-\theta$), resulting in a net magnetic flux of $\Delta\theta = 2\theta$ (see Fig. 13). One can tune the non-Hermiticity coefficient, γ, from zero to C, and the eigenvalue becomes nondispersive. This scenario resembles the formation of an Aharonov-Bohm cage with a phase difference $\Delta\theta = \pi$. Further, the system becomes defective with the appearance of exceptional points.

Next, we consider the stub lattice with a balanced non-Hermitian coupling, resulting in zero net flux. The coupling through each leg of the lattice manifesting balanced gain and loss has the following form, $\kappa_1 = C$, $\kappa_2 = 0$ and $\kappa_3 = \kappa_4^* = C + i\gamma$. Consequently, the non-Hermiticity causes the broadening of the two dispersive bands through the tuning of the effective coupling of the system. With increasing γ, the lower band merges with the flat band, giving rise to an exceptional point with the critical momentum, $k = k_c = \cos^{-1}(1 - 5/(2 + 2\gamma^2/C^2))$ [17].

APPENDIX K: DECIMATION SCHEME FOR A FIVE-SITE MODEL

Next, we discuss the nature of the band structure of a five-site parity-time (PT) symmetric Q1D Lieb lattice model in the presence of non-Hermiticity. In particular, the model features a non-Hermitian flat band and CLS in real space as a result of local destructive interference of the wavefunctions. The Lieb photonic lattice can be realized as an array of periodically arranged evanescently coupled waveguides, which consists five sites per unit cell [57–60]. The Hamiltonian of interest for the non-Hermitian Lieb lattice model can be written in the tight-binding basis as

$$\begin{aligned}
H = \sum_n &(\varepsilon_a a_n^\dagger a_n + \varepsilon_b b_n^\dagger b_n + \varepsilon_c c_n^\dagger c_n + \varepsilon_d d_n^\dagger d_n + \varepsilon_e e_n^\dagger e_n)\\
&+ a_n^\dagger(\tilde{t_1}b_n + \tilde{t_2}b_{n-1} + tc_n) + e_n^\dagger(\tilde{t_2}d_n + \tilde{t_1}d_{n-1} + tc_n) + \text{H.c.},
\end{aligned}$$

where $\{a_n^\dagger, b_n^\dagger, c_n^\dagger, d_n^\dagger, e_n^\dagger\}$ and $\{a_n, b_n, c_n, d_n, e_n\}$ are the fermionic creation and annihilation operator in the nth unit cell for sublattice $\{A, B, C, D, E\}$, respectively. The parameters t, $\tilde{t_1}$, and $\tilde{t_2}$ are the coupling coefficients between different sites that can, in principle, be nonreciprocal to account for the non-Hermiticity. Here, let us consider that the non-Hermiticity is introduced as an on-site gain and loss term similar to the flat-band model, as depicted in Fig. 4 the main text. The corresponding Hamiltonian can be expressed in momentum space by Fourier transforming the operators to obtain

$$H_k = \begin{pmatrix} \varepsilon_a & t_1 + t_2e^{-ikl} & t & 0 & 0 \\ t_1 + t_2e^{ikl} & \varepsilon_b & 0 & 0 & 0 \\ 0 & 0 & \varepsilon_c & 0 & t \\ 0 & 0 & 0 & \varepsilon_d & t_2 + t_2e^{ikl} \\ 0 & 0 & t & t_2 + t_1e^{-ikl} & \varepsilon_e \end{pmatrix}. \qquad \text{(K1)}$$

In the main text, we evaluated the dispersion relations of the same model using an exact real-space decimation method to eliminate the A and E sites. However, here, we shall use a similar strategy to decimate out the $\{B, C, D\}$ subset of sites, keeping $\{A, E\}$ intact to establish that the decimation path is not unique. We can write the difference equations using Eq. (B1) for the real-space system as

$$\begin{aligned}
(E-\varepsilon_a)\phi_a &= t_1\phi_b + t_2\phi_{b'} + t\phi_c,\\
(E-\varepsilon_c)\phi_c &= t\phi_a + t\phi_e,\\
(E-\varepsilon_e)\phi_e &= t_2\phi_d + t_1\phi_{d'} + t\phi_c,
\end{aligned}$$

$$(E-\varepsilon_b)\phi_b = t_1\phi_a + t_2\phi_{al},$$
$$(E-\varepsilon_d)\phi_d = t_2\phi_e + t_1\phi_{el},$$
$$(E-\varepsilon_b)\phi_{b'} = t_2\phi_a + t_1\phi_{ar},$$
$$(E-\varepsilon_d)\phi_{d'} = t_1\phi_e + t_2\phi_{er}. \tag{K2}$$

Eliminating ϕ_c from Eq. (K2), we get the following transformed equations

$$(E-\varepsilon'_a)\phi_a = t_1\phi_b + t_2\phi'_b + t_{co}\phi_e,$$
$$(E-\varepsilon'_e)\phi_e = t_2\phi_d + t_1\phi'_d + t_{co}\phi_a, \tag{K3}$$

where $\varepsilon'_{a/e} = \varepsilon_{a/e} + t_{co}$ and $t_{co} = \frac{t^2}{E-\varepsilon_c}$. Therefore, the decimated lattice does not possess the site C; however, all the information regarding it is encoded in the remaining decimated lattice model with four sites per unit cell. Next, we shall decimate the sites B and D to obtain an effective two-site lattice problem model without losing any information about the original system. The difference equations read

$$(E-\Delta_a)\phi_a = u\phi_{al} + u\phi_{ar} + t_{co}\phi_e,$$
$$(E-\Delta_e)\phi_e = d\phi_{el} + d\phi_{er} + t_{co}\phi_a. \tag{K4}$$

In the above Eq. (K4), the parameters have the following form, $\Delta_a = \varepsilon'_a + \frac{t_1^2+t_2^2}{E-\varepsilon_b}$, $\Delta_e = \varepsilon'_e + \frac{t_1^2+t_2^2}{E-\varepsilon_d}$, $u = \frac{t_1t_2}{E-\varepsilon_b}$, and $d = \frac{t_1t_2}{E-\varepsilon_d}$. In particular, the decimated system features a simplified uniform ladder network with energy-dependent decimated coupling and renormalized on-site potential. The Hamiltonian reads

$$\begin{pmatrix} \Delta_a + 2u\cos k & t_{co} \\ t_{co} & \Delta_e + 2d\cos k \end{pmatrix}. \tag{K5}$$

We show that this two-level system is a caricature of the original five-site system described by the Hamiltonian in Eq. (K1) and mimics the dispersion and concomitant phase transition in the presence of exceptional points without losing any information about the original system. Next, we extend our analysis and further simplify the ladder in order to transform it into two decoupled chains via a basis transformation to bring forth the rich physics of the system. We show that the model naturally gives rise to the SSH dispersion and explains the presence of CLS. We start from the one-dimensional real-space tight-binding model with two orbitals, A and E, in a unit cell for the momentum-space Hamiltonian in Eq. (K5). We can write the tight-binding Hamiltonian for the ladder network as

$$H = \sum_m \epsilon_m c_m^\dagger c_m + h\left(\sum_m c_m^\dagger c_{m+1} + \text{c.c.}\right), \tag{K6}$$

where $c_m = \begin{pmatrix} c_{m,1} \\ c_{m,2} \end{pmatrix}$, $\epsilon_m = \begin{pmatrix} \Delta_a & t_{co} \\ t_{co} & \Delta_e \end{pmatrix}$, $h = \begin{pmatrix} u & 0 \\ 0 & d \end{pmatrix}$ and $c^\dagger_{m,j}(c_{m,j})$ is the fermionic creation (annihilation) operator at the nth site of the jth arm. The parameters t_{co} and u/d are, respectively, vertical and horizontal hopping integrals of the decimated uniform ladder network. Here, the eigenbasis for the ladder network is defined by the real-space vector

$$\psi_n = \begin{pmatrix} \psi_{n,1} \\ \psi_{n,2} \end{pmatrix}. \tag{K7}$$

In this basis, the difference equation reads

$$[E-\epsilon_n]\psi_n = h[\psi_{n+1} - \psi_{n-1}]. \tag{K8}$$

In the main text we have considered, $\varepsilon_a = \varepsilon_e$ and $\varepsilon_b = \varepsilon_d$ (so, $u = d$), which changes the form of h to $h = \begin{pmatrix} u & 0 \\ 0 & u \end{pmatrix}$. Next, we use a similarity transformation to diagonalize the uniform ladder network system with a suitable change of basis going from the basis $\psi_n \equiv (\psi_{n,1}, \psi_{n,2})$ to a new basis $\phi_n \equiv (\phi_{n,1}, \psi_{n,2})$, where

$$\phi_i \equiv \sum_{j=1}^{2} (M^{-1})_{ij}\psi_j. \tag{K9}$$

The matrix M diagonalizes the system, and eventually, we can write two decoupled sets of difference equations as follows

$$[E-\epsilon_+]\phi_{n,1} = u\,\phi_{n+1,1} + u\,\phi_{n-1,1}, \tag{K10}$$

and

$$[E-\epsilon_-]\phi_{n,2} = u\,\phi_{n+1,1} + u\,\phi_{n-1,1}. \tag{K11}$$

Here $\epsilon_\pm = \Delta_a \pm t_{co}$, where $\Delta_a = \Delta_e$. Interestingly, we obtain two independent linear chains in terms of the decimated parameters. The intricacy of these decoupled chains can mimic the original dispersion that essentially gives rise to a flat band, as also obtained in the main text.

[1] E. J. Bergholtz, J. C. Budich, and F. K. Kunst, Rev. Mod. Phys. **93**, 015005 (2021).
[2] Y. Ashida, Z. Gong, and M. Ueda, Adv. Phys. **69**, 249 (2020).
[3] R. El-Ganainy, K. G. Makris, M. Khajavikhan, Z. H. Musslimani, S. Rotter, and D. N. Christodoulides, Nat. Phys. **14**, 11 (2018).
[4] X. Zhang, T. Zhang, M.-H. Lu, and Y.-F. Chen, Adv. Phys.: X **7**, 2109431 (2022).
[5] A. Banerjee, R. Sarkar, S. Dey, and A. Narayan, J. Phys.: Condens. Matter **35**, 333001 (2023).
[6] K. Kawabata, K. Shiozaki, M. Ueda, and M. Sato, Phys. Rev. X **9**, 041015 (2019).
[7] K. Ding, C. Fang, and G. Ma, Nat. Rev. Phys. **4**, 745 (2022).
[8] Z. Gong, Y. Ashida, K. Kawabata, K. Takasan, S. Higashikawa, and M. Ueda, Phys. Rev. X **8**, 031079 (2018).
[9] K. Zhang, Z. Yang, and C. Fang, Phys. Rev. Lett. **125**, 126402 (2020).
[10] S. Yao and Z. Wang, Phys. Rev. Lett. **121**, 086803 (2018).
[11] S. Yao, F. Song, and Z. Wang, Phys. Rev. Lett. **121**, 136802 (2018).

[12] L. Feng, Z. J. Wong, R.-M. Ma, Y. Wang, and X. Zhang, Science **346**, 972 (2014).

[13] S. Weidemann, M. Kremer, T. Helbig, T. Hofmann, A. Stegmaier, M. Greiter, R. Thomale, and A. Szameit, Science **368**, 311 (2020).

[14] H. Zhao, X. Qiao, T. Wu, B. Midya, S. Longhi, and L. Feng, Science **365**, 1163 (2019).

[15] S. Longhi, D. Gatti, and G. D. Valle, Sci. Rep. **5**, 13376 (2015).

[16] K. Wang, A. Dutt, C. C. Wojcik, and S. Fan, Nature (London) **598**, 59 (2021).

[17] D. Leykam, S. Flach, and Y. D. Chong, Phys. Rev. B **96**, 064305 (2017).

[18] W. X. Teo, L. Li, X. Zhang, and J. Gong, Phys. Rev. B **101**, 205309 (2020).

[19] C.-X. Guo, S. Chen, K. Ding, and H. Hu, Phys. Rev. Lett. **130**, 157201 (2023).

[20] Q. Zhang, L. Zhao, X. Liu, X. Feng, L. Xiong, W. Wu, and C. Qiu, Phys. Rev. Res. **5**, L022050 (2023).

[21] W. Tang, K. Ding, and G. Ma, Natl. Sci. Rev. **9**, nwac010 (2022).

[22] K. Wang, A. Dutt, K. Y. Yang, C. C. Wojcik, J. Vučković, and S. Fan, Science **371**, 1240 (2021).

[23] J. A. Ashraff and R. B. Stinchcombe, Phys. Rev. B **37**, 5723 (1988).

[24] A. Chakrabarti, S. N. Karmakar, and R. K. Moitra, Phys. Rev. Lett. **74**, 1403 (1995).

[25] A. Bandyopadhyay and D. Jana, Rep. Prog. Phys. **83**, 056501 (2020).

[26] L. P. Kadanoff, Phys. Phys. Fiz. **2**, 263 (1966).

[27] A. Jagannathan, Phys. Rev. Lett. **92**, 047202 (2004).

[28] M. C. Angelini and G. Biroli, Proc. Natl. Acad. Sci. USA **114**, 3328 (2017).

[29] M. Koch-Janusz and Z. Ringel, Nat. Phys. **14**, 578 (2018).

[30] V. Kozii and L. Fu, arXiv:1708.05841.

[31] H. Carmichael, *An Open Systems Approach to Quantum Optics: Lectures presented at the Université Libre de Bruxelles, October 28 to November 4, 1991*, Vol. 18 (Springer Science & Business Media, 2009).

[32] S. Lieu, Phys. Rev. B **97**, 045106 (2018).

[33] L. Herviou, J. H. Bardarson, and N. Regnault, Phys. Rev. A **99**, 052118 (2019).

[34] H. C. Wu, L. Jin, and Z. Song, Phys. Rev. B **103**, 235110 (2021).

[35] L. Jin and Z. Song, Phys. Rev. B **99**, 081103(R) (2019).

[36] F. K. Kunst, E. Edvardsson, J. C. Budich, and E. J. Bergholtz, Phys. Rev. Lett. **121**, 026808 (2018).

[37] F. Song, S. Yao, and Z. Wang, Phys. Rev. Lett. **123**, 170401 (2019).

[38] K. Esaki, M. Sato, K. Hasebe, and M. Kohmoto, Phys. Rev. B **84**, 205128 (2011).

[39] V. M. M. Alvarez, J. E. B. Vargas, and L. E. F. F. Torres, Phys. Rev. B **97**, 121401(R) (2018).

[40] D. S. Borgnia, A. J. Kruchkov, and R.-J. Slager, Phys. Rev. Lett. **124**, 056802 (2020).

[41] A. Banerjee, R. Jaiswal, M. Manjunath, and A. Narayan, Proc. Natl. Acad. Sci. USA **120**, e2302572120 (2023).

[42] R. Jaiswal, A. Banerjee, and A. Narayan, New J. Phys. **25**, 033014 (2023).

[43] H. Eleuch and I. Rotter, Phys. Rev. A **95**, 022117 (2017).

[44] Y. Xiong, J. Phys. Commun. **2**, 035043 (2018).

[45] L. Xiao, T. Deng, K. Wang, G. Zhu, Z. Wang, W. Yi, and P. Xue, Nat. Phys. **16**, 761 (2020).

[46] T. Helbig, T. Hofmann, S. Imhof, M. Abdelghany, T. Kiessling, L. Molenkamp, C. Lee, A. Szameit, M. Greiter, and R. Thomale, Nat. Phys. **16**, 747 (2020).

[47] F. K. Kunst and V. Dwivedi, Phys. Rev. B **99**, 245116 (2019).

[48] K. Yokomizo and S. Murakami, Phys. Rev. Lett. **123**, 066404 (2019).

[49] Z. Yang, K. Zhang, C. Fang, and J. Hu, Phys. Rev. Lett. **125**, 226402 (2020).

[50] S. M. Rafi-Ul-Islam, Z. B. Siu, H. Sahin, C. H. Lee, and M. B. A. Jalil, Phys. Rev. Res. **4**, 043108 (2022).

[51] Y.-M. Hu, H.-Y. Wang, Z. Wang, and F. Song, Phys. Rev. Lett. **132**, 050402 (2024).

[52] C. M. Bender and S. Boettcher, Phys. Rev. Lett. **80**, 5243 (1998).

[53] S. Datta, *Electronic Transport in Mesoscopic Systems* (Cambridge University Press, Cambridge, 1997).

[54] Q. Li, J.-J. Liu, and Y.-T. Zhang, Phys. Rev. B **103**, 035415 (2021).

[55] Y. Li and C. Argyropoulos, Phys. Rev. B **99**, 075413 (2019).

[56] A. Soori, M. Sivakumar, and V. Subrahmanyam, J. Phys.: Condens. Matter **35**, 055301 (2023).

[57] R. A. Vicencio, C. Cantillano, L. Morales-Inostroza, B. Real, C. Mejía-Cortés, S. Weimann, A. Szameit, and M. I. Molina, Phys. Rev. Lett. **114**, 245503 (2015).

[58] C. E. Whittaker, E. Cancellieri, P. M. Walker, D. R. Gulevich, H. Schomerus, D. Vaitiekus, B. Royall, D. M. Whittaker, E. Clarke, I. Iorsh *et al.*, Phys. Rev. Lett. **120**, 097401 (2018).

[59] X. Liu, S. Xia, E. Jajtić, D. Song, D. Li, L. Tang, D. Leykam, J. Xu, H. Buljan, and Z. Chen, Nat. Commun. **11**, 1586 (2020).

[60] S. Xia, C. Danieli, Y. Zhang, X. Zhao, H. Lu, L. Tang, D. Li, D. Song, and Z. Chen, APL Photonics **6**, 126106 (2021).

[61] E. H. Lieb, Phys. Rev. Lett. **62**, 1201 (1989).

[62] B. Sutherland, Phys. Rev. B **34**, 5208 (1986).

[63] A. Banerjee, S. S. Hegde, A. Agarwala, and A. Narayan, Phys. Rev. B **105**, 205403 (2022).

[64] W. A. Benalcazar, B. A. Bernevig, and T. L. Hughes, Phys. Rev. B **96**, 245115 (2017).

[65] W. A. Benalcazar, B. A. Bernevig, and T. L. Hughes, Science **357**, 61 (2017).

[66] C. Martínez-Strasser, M. Herrera, G. Palumbo, F. K. Kunst, and D. Bercioux, Adv Quantum Technol. **7**, 2300225 (2023).

[67] H. Schomerus, Phys. Rev. Res. **5**, 043224 (2023).

[68] B. A. Bhargava, I. C. Fulga, J. van Den Brink, and A. G. Moghaddam, Phys. Rev. B **104**, L241402 (2021).

[69] F. Schindler and A. Prem, Phys. Rev. B **104**, L161106 (2021).

[70] A. Panigrahi, R. Moessner, and B. Roy, Phys. Rev. B **106**, L041302 (2022).

[71] N. Chadha, A. G. Moghaddam, J. v. d. Brink, and C. Fulga, Phys. Rev. B **109**, 035425 (2024).

[72] A. Amir, N. Hatano, and D. R. Nelson, Phys. Rev. E **93**, 042310 (2016).

[73] S. Manna and B. Roy, Commun. Phys. **6**, 10 (2023).

[74] B. Zhou, R. Wang, and B. Wang, Phys. Rev. B **102**, 205116 (2020).

[75] S. Rahul and S. Sarkar, Sci. Rep. **12**, 6993 (2022).

[76] Q. Lin, T. Li, L. Xiao, K. Wang, W. Yi, and P. Xue, Phys. Rev. Lett. **129**, 113601 (2022).

[77] J. Pi and R. Lü, J. Phys.: Condens. Matter **33**, 345601 (2021).

[78] A. Hegde, A. Kumar, A. Agarwala, and B. Muralidharan, Reson. **27**, 1913 (2022).
[79] C. Yin, H. Jiang, L. Li, R. Lü, and S. Chen, Phys. Rev. A **97**, 052115 (2018).
[80] J. Y. Lee, J. Ahn, H. Zhou, and A. Vishwanath, Phys. Rev. Lett. **123**, 206404 (2019).
[81] T. Bessho and M. Sato, in APS March Meeting 2021, abstract id.R46.008 (2021).